National Library of Canada

Acquisitions and Bibliographic Services Branch

395 Wellington Street
Ottawa, Ontario
K1A 0N4

Bibliothèque nationale du Canada

Direction des acquisitions et des services bibliographiques

395, rue Wellington
Ottawa (Ontario)
K1A 0N4

Your file Votre référence

Our file Notre référence

NOTICE

The quality of this microform is heavily dependent upon the quality of the original thesis submitted for microfilming. Every effort has been made to ensure the highest quality of reproduction possible.

If pages are missing, contact the university which granted the degree.

Some pages may have indistinct print especially if the original pages were typed with a poor typewriter ribbon or if the university sent us an inferior photocopy.

AVIS

La qualité de cette microforme dépend grandement de la qualité de la thèse soumise au microfilmage. Nous avons tout fait pour assurer une qualité supérieure de reproduction.

S'il manque des pages, veuillez communiquer avec l'université qui a conféré le grade.

La qualité d'impression de certaines pages peut laisser à désirer, surtout si les pages originales ont été dactylographiées à l'aide d'un ruban usé ou si l'université nous a fait parvenir une photocopie de qualité inférieure.

Canada

BENDING FATIGUE OF CANCELLOUS BONE SCREWS USED IN ANTERIOR SPINE SURGERY

by

Stephen Gregory Gilbert

A thesis submitted to the

School of Graduate Studies and Research

in partial fulfilment of the requirements for the degree of

M.A.Sc. in Mechanical Engineering

DEPARTMENT OF MECHANICAL ENGINEERING

UNIVERSITY OF OTTAWA

OTTAWA, ONTARIO

May, 1993

ISBN 0-315-89628-0

Canada

UNIVERSITÉ D'OTTAWA
UNIVERSITY OF OTTAWA

ACKNOWLEDGEMENTS

Dr. S. Mirza Department Mechanical of Engineering, University of Ottawa, Mr. Don Raizenne, Mr. Tom Benak, Mr. Nick Bellinger and Mr. Ray Dainty, Institute for Aerospace Research, National Research Council, Dr. Don Chow, Department of Orthopaedic Surgery, Ottawa Civic Hospital, and Mr. Ray Desjardins, Terray Corporation, Arnprior Ontario.

ABSTRACT

Bending fatigue has been noted in early clinical results of anterior spinal fixation using standard 6.5mm outside diameter (3.2mm inside diameter) cancellous bone screws. Fractography was used to qualify and quantify the failure mode. Fracture mechanics was used to determine the load level from the fractographic findings. These results were used in a test program to reproduce the fatigue failures seen in-vivo. The validity of the experimental model was investigated by varying test coupon parameters, testing the modified specimens and comparing the results to those predicted.

TABLE OF CONTENTS

APPENDICES

1.0 Light Micrographs of Failed Implants

2.0 SEM of Failed Implants

3.0 Vickers Hardness Measurements

4.0 Certificate of Test for 316L

5.0 Sample Calculations

6.0 Light Micrographs of 3.2mm test coupons

7.0 SEM of 3.2mm test specimens

8.0 Light micrographs of 4.0mm specimens

9.0 Effect of Cold Work in Tensile Properties of 316L

LIST OF FIGURES

LIST OF SYMBOLS

a=crack length

A=cross sectional area

A_t=tensile stress area

d=nominal diameter

d_e=effective diameter

d_m=minor diameter

d_p=pitch diameter

d_M=major diameter

$\frac{da}{dN}$=crack propagation rate

$F_{B,I,2}$=two dimensional constant for shaft under bending

$F_{T,I,2}$=two dimensional constant for shaft under tension

$F_{B,I,3}$=three dimensional constant for shaft under bending

I=moment of inertia

$F_{T,I,3}$=three dimensional constant for shaft under tension

K=stress concentration factor

K_f=fatigue stress concentration factor

K_t=theoretical stress concentration factor

$\Delta K_{B,I,3}$=three dimensional fluctuating stress intensity factor

ΔK=Stress intensity factor

l=length

M=moment

N=number of threads per inch

P=applied load

q=notch sensitivity factor

r=radius

r_p=plastic zone size radius

$\Delta\sigma$=fluctuating stress

σ_{av}=*average stress*

σ_e=*endurance limit*

σ_{max}=*maximum stress*

σ_{min}=*minimum stress*

σ_{nom}=*nominal stress*

σ_r=*stress range*

σ_R=*equivalent completely reversed stress*

σ_{ys}=*yield strength*

σ_{ult}=*ultimate tensile strength*

t=thickness

TCE=test coupon elongation

τ=*shear stress*

y_{max}=*maximum deflection*

y=deflection

LIST OF TABLES

GLOSSARY

austenite - Face centered cubic iron

bone graft - bone used to augment fractued bone ; usually taken from another location in the body

cancellous bone - spongy or lattice-like structure found predominantly in vertebrae

cord compromize - the amount of displacment of bone into the spianl cord region of the vertebrae

cortical bone - dense bone found throughout the body which varies in thickness from the 1mm shell surrounding vertebrae, to several inches thick in the femur or thigh bone

surgical construct - an implant and the bone to which it is attached

in-vivo -pertaining to the living body

in-vitro - pertaining to the deceased body

slip - hexagonal metals and cubic metals and their unordered alloys deform predominantly by plastic shear or slip where one plane of atoms slides over the next adjacent plane. Shear deformation occurs even when compression or tension stresses are applied, because these stresses may be resolved into shear stresses.

1 INTRODUCTION

The human spine is a segmented structure composed of 29 vertebrae, 7 of which are fused and make up the sacrum or tail bone as shown Figure 1. The spine is divided anatomically into four regions ; cervical (neck), thoracic (ribs), lumbar and sacral. The majority of surgical procedures are performed in the lumbar region. The lumbar spine consists of 5 vertebral bodies located between the sacrum and the thoracic regions as shown Figure 2. Each vertebrae is composed of a thin outer shell (approximately 1mm thick) of cortical bone and a porous interior composed of cancellous bone. Figure 3 is a computer tomographic (CT) scan of a normal lumbar vertebral body showing the distinct triangular region which surrounds the spinal cord. Trauma and/or other disease processes can cause fracture or collapse of a vertebral body resulting in bone fragments invading the spinal cord region. The CT scan shown in Figure 4 is classified as a burst fracture which, depending on the degree of cord compromise, may result in some type of partial or complete paralysis.

The Contoured Anterior Spinal Plate (CASP) was designed for treatment of anterior burst fractures of the lumbar spine[5]. The system consists of various sizes of plates as shown in Figure 5 and screws which have a major diameter of 6.5mm (.256") and a minor diameter of 3.2mm (.126") as shown in Figure 6. The bottom of the screw head has

a circular profile (7.9mm=.312" dia). The plate holes are also circular with a slightly larger diameter (8.0mm=.315") which allows the screw to sweep through an included angle of approximately 26 degrees.

The surgical procedure consists of removing the fragmented vertebrae and the upper and lower intervertebral discs. The surgical construct consists of bone graft which is held in place by a stainless steel plate attached to the inferior and superior vertebral bodies with stainless steel screws as shown in Figure 7. The plate is mounted on the side (laterally) of the spine with the screws usually engaging the full width of the vertebral body as shown in Figure 8. Black et.al.[5] recommend that the implant is removed after the bone graft has healed.

The standard industry method for producing cancellous bone screws consists of cutting the thread form from round bar stock, either by single point cutting or thread chasing, followed by superfinishing (8-2 microinch) by electropolishing and passivation in a nitric acid solution[1]. It should be noted that these screws cannot be rolled due to the large ratio of major to minor diameter and the relatively thin thread profile.

Bone responds to the loads applied upon it or the lack there of. Thus bone which is not used tends to be resorbed by the body as in the case of astronauts. Bone which is

highly loaded tends to be stronger and the body tends to accumulate more bone in these areas. Normal bone regenerates continuously at a relatively slow rate. In an injured bone, the healing and regenerative processes are highly activated[8]. One important precondition for bone healing is immobilization. Bone tissue tolerates only minimal amounts of motion, particularly during repair[8]. Implants are not intended to support the same load as the healthy bone. Thus the function of an implant is to hold the ends of the bone in close proximity so that healing is promoted while allowing adequate loading to prevent bone resorption. As the bone heals, its load carrying capacity increases and thus the need for the implant decreases. This phenomenon has led researchers to investigate the use of biodegradable implants whose strength and stiffness reduces at approximately the same rate as the bone heals[27].

Early clinical results of the CASP system[10] have shown screw breakage in several cases as shown in Figure 9. The elapsed time from implantation to screw breakage was approximately one year suggesting a fatigue type failure. Many different variables contribute to the loading conditions including, patient weight, activity level, age, and bone and muscle condition. Given the random nature of these variables, it is difficult to predict the load levels that an implant would be subjected to. By performing post failure analysis using optical and scanning electron microscopes one can study the failure surface and determine crack initiation sites, crack propagation rates and final fracture zone size[7]. An

estimate of the applied load can be made using fracture mechanics principles. These load levels may then be used to attempt to reproduce the failures seen clinically. Once the failure mode has been reproduced, design improvements can be made and tested prior to implantation.

The loading a screw is subjected to is a combination of tension, shear and bending[13]. By analyzing the potential stresses induced in each load direction, one may estimate the relative contribution of each component. In a previous study[13], the author performed pullout tests of cancellous bone screws placed in vertebral bodies. The orientation of the screws in the vertebrae was the same as that employed in the use of the CASP system. The direction of loading was along the longitudinal axis of the screw. Of the ten specimens tested, the maximum yield strength was found to be 30 Kg. This was the maximum load applied to the screw before permanent deformation of the bone took place. The induced tensile stress was 57.2 MPa assuming no stress concentration. Given that the endurance limit of the material is approximately 731MPa, the tensile component is relatively small compared to that required to cause fatigue failure.

Until recently, it was generally believed that corrosion played an important role in the performance of 316L stainless steel implants as observed in retrieved implants and experimental test conditions[22]. There is no question that body fluids contain the necessary

electrolytes for corrosion to occur, however, the materials used and the conditions found in the body are difficult to interpret and reproduce.

It is now generally believed that stress corrosion cracking failure mode has been implicated in the in-vivo failure of orthopaedic implants because of the apparent fractographic similarities between implant failures observed in-vivo and those shown in stress corrosion cracking investigations of stainless steels[22]. Gilbertson[14] presented some work showing that even at 66 degrees celsius and a pH of 2 to 3 with hydrochloric acid, 316 LVM (low carbon, vacuum melt) four point bend specimens did not fail in 15000 hours of testing. Another study showed that 316L would not fail by stress corrosion cracking in a physiological saline environment[22].

The common solution chosen to perform environmental fatigue testing is Ringer's solution (0.9% NaCl in water, pH=7.0) at 37 degrees celsius. Given the dependence of corrosion fatigue on test frequency[7], tests for human loading are generally conducted at 1 hertz. Most of the studies claiming corrosive effects were either done at higher frequencies, lower pH and/or nonpassivated surfaces. Tests which duplicated in-vivo material condition (electropolished and passivated), fluid and load frequency found no evidence of corrosion in either the static or slow strain rate testing[22]. The integrity of the implant surface passivation was monitored using open circuit potentials. The tested

materials tended to passivate in Ringer's solution under static conditions but under cyclic loading, the potentials decline indicating the destruction of the passive film[19]. These results suggest that during periods of activity, the passive film is broken down while during periods of rest, the passive film regenerates (this is analogous to the general human pattern of sleep followed by daily activity). This is perhaps why more rigorous fractographic methods do not show evidence of stress corrosion cracking or corrosion fatigue.

Components which undergo fatigue loading are subjected to constant or variable amplitude loading. The type of load spectrum the human body undergoes is of variable amplitude and frequency. Several fatigue loading spectra have been developed for aeronautical applications[21], however, the author is unaware of any reported in the literature for the human body. Until such time as representative loading spectra are developed for the human body, fatigue testing will continue to be performed under constant amplitude conditions.

Constant amplitude bending fatigue testing in air is therefore justified and furthermore can be conducted at higher frequencies since corrosion effects are negligible in air.

2 THEORY

Fatigue is the progressive localized permanent change that occurs in a material that is subjected to repeated or fluctuating strains at stresses having a maximum value less than the tensile strength of the material. Fatigue fractures are caused by the simultaneous action of cyclic stress, tensile stress and plastic strain. If any of these is not present, fatigue cracking will not initiate and propagate[7]. The fracture surface that results from fatigue failure has a characteristic appearance that can be divided into three zones or progressive stages of fracture. Stage 1 crack initiation, Stage II crack propagation and Stage III final fracture[7].

Crack initiation occurs when alternating tensile stresses cause plastic deformation which cause the component to deform along slip planes that coincide with maximum shear stress - about 45 degrees from the direction of load in the case of axial loading-which results in slip steps on the surface. These steps correspond to stress raisers which initiate along the maximum shear planes and propagate normal to the maximum tensile stress component when the crack tip stress field becomes dominant[4]. A stage I fracture never extends over more than about two to five grains around the origin. There are usually no fatigue striations associated with a stage I fracture surface[7].

Under the repeated action of tensile stresses, the crack grows weakening the section. Variations in cyclic loads cause small ridges or "beach marks" to develop on the fracture surface ; they indicate the position of the advancing crack root at a given time. As the section gradually weakens, the crack grows faster, and the beach marks get farther apart, larger, and more distinct[28]. Fine striations are typical in stage II but frequently are seen only under high magnification[7]. Load spectrums and material properties greatly influence the visibility of beach marks.

Final fast fracture occurs when the cross section is unable to sustain the applied load. The surface appearance can be brittle or ductile or a combination of the two[7].

2.1 Features Revealed by Macroscopy

Examination of fatigue-fracture surfaces usually begins visually or by low magnification light microscope. The crack origin can best be found by viewing the fracture surface at low magnifications (25 to 100 diameters). The most characteristic feature usually found on fatigue fracture surfaces are beach marks which are centered around a common point that corresponds to the fatigue-crack origin as shown in Figure 10. Beach marks can occur as a result of changes in loading frequency or by oxidation of the fracture surface during periods of crack arrest from intermittent service of the part

or component[7]. In laboratory fatigue testing, load applications are usually uniform, and beach marks often fail to appear[28].

When fatigue originates in several locations of a filleted shaft, the juncture of progressing fractures usually result in "ratchet marks" as shown in Figure 11. The number of ratchet marks usually increase with increasing stress and stress concentration.

The notch sensitivity of the material sometimes affects the appearance of a fracture. A fatigue crack tends to grow more rapidly in a notch sensitive material at the highly stressed surface. In rotating bending, beach marks curve away from the origin because the rate of crack growth is greater along the periphery than toward the interior. Conversely, a crack in a less notch sensitive material, such as annealed steel, progresses at a lower rate along the periphery producing a concave pattern around the origin.

The final fracture zone of a fatigue-fracture surface often is fibrous, resembling the fracture surface of impact or fracture-toughness test specimens of the same material. The size of the final-fracture zone depends on the magnitude of the loads and its shape depends on the shape, size and direction of loading of the fractured part. In tough materials, with thick round sections, the final fracture zone will consist of a fracture by two distinct modes: (a) tensile fracture (plane strain mode) extending from the fatigue

zone and in the same plane, and (b) shear fracture (plane stress mode) at 45 degrees to the surface of the part bordering the tensile fracture[7].

2.2 Features Revealed by Microscopy

In the electron microscope examination of fatigue-fracture surfaces, the most prominent features found are patches of finely spaced parallel marks, called fatigue striations. The fatigue striations are oriented perpendicular to the microscopic direction of crack propagation and, with uniform loading, generally increase in spacing as they progress from the origin of fatigue. Each striation is the result of a single cycle of stress (but every stress cycle does not necessarily produce a striation) and striation spacing is strongly dependant on the level of applied loading. The clarity of the striations depends on the ductility of the material. Striations are more visible at stress levels higher than the fatigue limit ; also they are more visible in ductile materials[7].

2.3 Hardness Testing

Hardness is defined as the resistance of a material to penetration of its surface. As might be expected, the hardness and the strength of a material are closely related. The three most common procedures used to measure hardness are Brinell, Rockwell, and

Vickers. The Vickers test uses a diamond pyramid with a very light load thus enabling the hardness to be measured in a microscopic area[26]. The Vickers number is obtained by dividing the applied load in kilograms-force by the surface area of the indentation in square millimetres computed from the mean of the measured diagonals of the indentation. The spacing between indentations shall be such that the distance between any two indentations is greater than twice the extent of any stress deformation (cold working, butterfly fractures, etc.) that may occur as a result of the indentation process so that there shall be no overlap of the deformation between two indentations[3].

2.4 Factors Affecting Fatigue Life

Factors which affect fatigue life include the type of loading (uniaxial, bending, torsional), the shape of the loading curve (sinusoidal, sawtooth), the frequency of loading, the loading pattern (constant or variable amplitude), magnitude of the stresses, the part size, fabrication method and surface roughness, operating temperature and environment[7].

2.4.1 Type of Loading and Part Shape

Nucleation and growth of a fatigue crack and features on the surface are all strongly affected by the shape of the part and the type and magnitude of loading exerted

on the part. The different loading types include unidirectional bending, alternating bending, rotating bending, torsional loading and axial loading. A schematic representation of fatigue fractures produced in smooth and notched components with round, square and rectangular cross sections under various loading conditions at high and low nominal stress as shown in figure 10^7.

2.4.2 Shape of the Loading Curve

The shape of the loading curve only affects the fatigue behaviour of components exposed to corrosive environments[4].

2.4.3 Rate of Loading

For steel the fatigue strength is not affected between 200 and 5000 cycles per minute. At higher frequencies, fatigue limits appear to rise[28].

2.4.4 Constant versus Variable Amplitude

Changes in cyclic-load magnitude may result in retarded or accelerated fatigue-crack-growth rate. Fatigue life under constant amplitude testing is generally shorter than

the life obtained under random sequence load spectra. This occurs when the magnitude of the overload is such that the fatigue-crack-growth rate is retarded due to crack tip blunting[4].

2.4.5 Magnitude of Stresses

Fatigue analysis generally involves predicting the number of cycles to failure at a given stress magnitude. The relationship between the completely reversing applied stress and the number of cycles to failure is usually described as an SN diagram as shown in Figure 12. The relationship is linear when the stress is plotted versus the log of the number of cycles. Any combination of stress and cycles above the line will fail prematurely while below the line is considered safe for the given number of cycles. Materials such as steels exhibit an endurance limit which is the stress below which fatigue failure will not occur as seen in Figure 12.

The S-N curve usually reported for a given metal is often taken to represent a 50% probability of failure curve. Fatigue tests of a large number of fatigue specimens tested at a given stress level result in approximately 50% of the specimens failing above the line and 50% would fail below the line. The statistical nature of fatigue data may be represented either as a series of S-N curves representing different probabilities of failure

or as an S-N band as shown in Figure 13. Because of the large expense involved, S-N probability curves are seldom obtained[6].

2.4.6 Stress Concentrations

Stress concentrations result from sudden changes in material cross section which result in a stress raiser. The stress concentration factor K_t is the ratio of the maximum stress in the region of the notch to the corresponding nominal stress. For ductile materials, local yielding takes place under steady load if the yield point is exceeded at certain points of stress concentration. However, when the load is fluctuating and is below the yield strength, such local relief cannot be obtained, and a suitable stress concentration factor must be applied[25].

The fatigue notch factor K_f is the ratio of the fatigue strength of a smooth specimen to the fatigue strength of a notched specimen at the same number of cycles. The fatigue notch factor will vary with the position on the S-N curve and with mean shear stress. At high stress levels and short cycles, the factor is usually less than at lower stress levels. The notch sensitivity index, q, for a material is determined by comparing K_f and K_t for a specimen of a given shape and size[7]. For fatigue loading there is little or no evidence of yielding before complete fracture occurs. Thus the value of q is usually

between one half and one ; the value of unity generally occurs for harder material and one half for metals used in their softer condition[6].

$$q=\frac{K_f-1}{K_t-1} \qquad (1)$$

Values of q for different crack geometries, cross section and materials can be found in the reference material.

A single notch introduces a greater stress concentration effect than does a continuous thread because of the mutual relief afforded by adjacent threads[7]. Fatigue tests of threaded specimens and specimens having a single groove of the same dimensions showed considerably higher strength for the threaded specimens[18].

2.4.7 Overstress

The magnitude of the nominal stress on a cyclically loaded component is often measured by the amount of overstress - the amount by which the nominal stress exceeds the fatigue limit of the material used in the component. The number of load cycles that a component under low overstress can endure is high ; thus, the term high-cycle fatigue is often applied. Increasing the magnitude of the nominal stress has the following effects : (a) initiation of multiple cracks is more likely, (b) striation spacing is increased and (c)

the region of final fast fracture is increased in size. With very high overstress, low-cycle fatigue fractures are produced. The arbitrary but commonly accepted dividing line between high-cycle and low-cycle fatigue is considered to be about 100,000 cycles[2]. In practice, this distinction is made by determining whether the dominant component of the strain imposed during cyclic loading is elastic (high cycle) or plastic (low cycle) which in turn depends on the properties of the metal as well as the magnitude of the nominal stress[7].

2.4.8 Surface Finish

As fatigue cracks usually start at surface irregularities which introduce stress concentrations, the endurance limit of metals is very sensitive to surface finish. The endurance limit for a SAE 4063 steel was found to increase by 25% when the surface roughness was decreased from a circumferential grind (16-25 microinch) to a polished super finish (0.5-2.0 microinch)[26,28]. The fatigue life of electropolished specimens is about four fold greater than that of finely machined or ground specimens[15].

2.4.9 Combined Steady and Alternating Stresses

In many strength problems, the major components of stress are static with an alternating load superimposed. When the average stress is high, the material will safely

carry only a small additional range component. However, if the average stress is small, a larger range component can be permitted. To take care of the unlimited number of combinations of range and average stress, the line of failure must be used[25]. There have been several relations proposed to describe the effect of average stress including Soderberg, Gerber and Goodman as seen in Figure 14. For most metals, Soderberg relation yields conservative estimates of critical stress amplitude. The Gerber relation yields fairly good estimates for the stress amplitude for ductile materials. The Goodman relation gives good results for brittle materials whereas it is conservative for ductile materials[6]. A modified Goodman diagram is shown in Figure 15. The average stress is plotted versus the stress range. For a static stress, failure occurs at the ultimate stress. For a completely reversing stress (zero average), failure occurs at the endurance limit. For combinations of average stress and stress range, failure occurs at intermediate points. A stress concentration, if present, will apply only to the range component[25].

If the loading is such that the stress point falls outside the line of failure, fatigue failure can be expected after some finite number of stress reversals as shown in Figure 16. An equivalent completely reversing stress (zero average stress) which is equivalent to the combined load (stress average plus stress range) can be obtained from[25]

$$\sigma_R = \frac{K\sigma_r\sigma_{ult}}{\sigma_{ult}-\sigma_{av}} \tag{2}$$

where

$$\sigma_r = \frac{\sigma_{max}-\sigma_{min}}{2} = \frac{\sigma_{max}-R\sigma_{max}}{2} = \frac{\sigma_{max}(1-0.1)}{2} = 0.45\sigma_{max} \tag{3}$$

$$\sigma_{avg} = \frac{\sigma_{max}+\sigma_{min}}{2} = \frac{\sigma_{max}+R\sigma_{max}}{2} = \frac{\sigma_{max}(1+0.1)}{2} = 0.55\sigma_{max} \tag{4}$$

assuming a stress ratio of R=0.1. Substituting equations (3) and (4) into (2), the equivalent completely reversing stress can be written as

$$\sigma_R = \frac{0.45K\sigma_{max}\sigma_{ult}}{\sigma_{ult}-0.55\sigma_{max}} \tag{5}$$

where

$$K = \frac{\sigma_{max}}{\sigma_{nom}} \tag{6}$$

Solving for the maximum stress one obtains a quadratic equation of the form

$$0.45\sigma_{max}^2\sigma_{ult} + .55\sigma_{max}\sigma_{nom}\sigma_R - \sigma_{nom}\sigma_R\sigma_{ult} = 0 \tag{7}$$

from which the roots of the equation can be obtained.

For a circular shaft in bending,

$$\sigma_{nom}=\frac{32M}{\pi d^3} \tag{8}$$

where M is the applied moment and d is the nominal diameter. Substituting the results from equation (8) into equation (7), the maximum stress can be obtained.

Tests are made to determine the number of reversals L to failure at the completely reversed stress and the results plotted as shown in Figure 17[25]. The curve approaches asymptotically to the horizontal whose ordinate is the endurance limit. The curve plots as a straight line on log-log paperas shown in Figure 18. For finite life less than 1,000,000 cycles, the relationship between the completely reversed bending stress and the number of reversals to failure, L, is given by Basquin's equation[25]

$$A=\sigma_R L^B \tag{9}$$

where constants A and B are determined from experimental fatigue curves. Such curves are observed approximately to pass through the following points

$$at\ L=1000 \quad \sigma_R=.9\sigma_{ult} \tag{10}$$

$$at\ L=1,000,000 \quad \sigma_R=\sigma_e \tag{11}$$

Once A and B have been determined, one can solve for the completely reversed bending

stress for a given number of reversals L from the following

$$\log\sigma_R=\log\sigma_A-B\log L \qquad (12)$$

2.5 Fracture Mechanics

One of the limitations of the S-N diagram is that it does not distinguish between the crack initiation and crack propagation stages of fatigue. The fracture mechanics approach to fatigue is to distinguish between crack initiation and crack propagation by determining the number of cycles required to grow a crack from a critical size to final fracture[4]. Figure 19 shows the relation between the crack size "a" and the number of applied load cycles. The slope of the curve in the propagation stage is given by da/dN.

Linear elastic fracture mechanics (LEFM) analysis relates the stress field magnitude and direction in the vicinity of the crack tip to the nominal stress applied to the structural member, to the size, shape, and orientation of the crack and to material properties. The stress field ahead of a sharp crack can be characterized in terms of a single parameter, K, the stress intensity factor[4]. For an infinite plate subjected to a uniform tensile stress, the stress intensity factor is given by the equation

$$K=\sigma\times(\pi\times a)^{1/2} \qquad (13)$$

where sigma is the applied stress and a is the crack length[4]. For fatigue loading, (13) can

be rewritten as

$$\Delta K=\Delta\sigma\times(\pi\times a)^{1/2} \tag{14}$$

When K reaches a critical value, K_c, unstable crack propagation occurs. K_c is also known as the fracture toughness and is a material property. Other forms of equation (14) exist which depend on the specimen and crack geometry. Extensive stress-intensity-factor equations for various geometries and loading conditions are available in the literature[16,24]. The stress intensity for a circular arc edge crack in a bar under bending is given by

$$\Delta K=.73\Delta\sigma\sqrt{\pi a} \tag{15}$$

The stress intensity factor for a semi-elliptical surface crack in a shaft under bending is given by[16]

$$K_{B,I,3}=\sigma\sqrt{\pi b}F_{B,I,3} \tag{16}$$

where

$$F_{B,I,3}=F_{T,I,3}\frac{F_{B,I,2}}{F_{T,I,2}} \tag{17}$$

assuming b/d=c/W as shown in Figure 20. $F_{T,I,3}$ is a constant used to determine the stress intensity factor for a semi-elliptical surface crack for a shaft under tension and is given by

$$F_{T,I,3}=B\times\Lambda \tag{18}$$

where

$$B=1.122-0.23\beta-0.901\beta^2+0.949\beta^3-0.28\beta^4 \;;\beta=\frac{b}{a} \qquad (19)$$

and

$$\Lambda=1.0+0.157\lambda-0.634\lambda^2+4.59\lambda^3-6.628\lambda^4 \;;\lambda=\frac{a}{d} \qquad (20)$$

$F_{B,I,2}$ and $F_{T,I,2}$ are constants used to determine the stress intensity factor for a two dimensional edge crack in a strip under bending and tension respectively where

$$F_{B,I,2}=1.121-1.199\lambda+4.775\lambda^2-1.628\lambda^3-7.035\lambda^4+13.27\lambda^5 \qquad (21)$$

$$F_{T,I,2}=1.12-0.231\lambda+10.55\lambda^2-21.72\lambda^3+30.39\lambda^4 \qquad (22)$$

and

$$\lambda=\frac{C}{W} \qquad (23)$$

The applicability of LEFM is limited to plane strain conditions where the plastic zone size r_p is small compared to the material thickness t according to the following[11]

$$\frac{r_p}{t}<\frac{1}{50} \qquad (24)$$

where

$$r_p = \frac{1}{24\pi}\left(\frac{\Delta K}{\sigma_y}\right)^2 \qquad (25)$$

for fatigue loading. Fracture mechanics analysis dealing with cracking (as opposed to fracture) is sometimes referred to as subcritical fracture mechanics (SCFM), the final fracture event by cleavage being considered the critical condition. In general, the amount of plastic deformation involved in cracking is very small so that crack growth analysis uses LEFM concepts[8]. If the crack is close to critical (fracture) this may no longer true, but because by far the longest time is spent in the growth of much smaller cracks, it is justifiable to use LEFM to obtain the time for crack growth with good accuracy[8].

The log of the stress intensity factor (delta K) is also related to the log of the crack growth rate (da/dN) as shown in Figure 21. This curve is characteristic for the type of material under consideration. The data in Figure 21 indicate that conservative and realistic estimates of the fatigue crack propagation rates for austenitic steels in a room temperature air environment can be obtained from[4]

$$\frac{da}{dN} = 3.0 \times 10^{-10} (\Delta K_1)^{3.25} \qquad (26)$$

where a = inches and

$$K_1 = ksi\sqrt{inch} \qquad (27)$$

It should be noted that the condition of the 316 stainless used to obtain the data was 20 percent cold worked.

2.6 Analysis of Threaded Fasteners

A thread is defined by its major diameter(d), minor diameter(d_m), pitch and thread form. The pitch diameter (d_p) is the diameter at which the width of the thread is equal to the width of the space between threads. For symmetrical threads with a 60 degree included angle, the pitch diameter is given by[25]

$$d_p = d - .6495p \qquad (28)$$

A great many tensile tests of threaded rods have shown that an unthreaded rod having a diameter equal to the mean of the pitch and minor diameters will have the same tensile strength as the threaded rod. The area of this unthreaded rod is called the tensile-stress area A_t of the threaded rod[23]. For steels up to 100,000 psi ultimate strength

$$A_t = \frac{\pi}{4}\left(d - \frac{.9743}{n}\right)^2 \qquad (29)$$

where D is the major diameter, and n is the number of threads per inch[17]. The effective

diameter d_e can then be obtained from A_t. These formulae apply to symmetrical threads with a 60 degree included angle.

3 PURPOSE

The primary purpose of this work is to perform post failure analysis of failed screws to determine the failure mode and estimate the applied load using fracture mechanics principles. The results of this investigation will be used to attempt to reproduce the fracture pattern found in-vivo and compare these results to the failed screws. Finally, the validity of the experimental model will investigated to see if it will produce predictable results by varying the screw design and subjecting new test coupons to the experimental model.

4 APPARATUS

4.1 Failure Investigation of Implanted Screws

An Olympus S2H-1LLD optical microscope with a polaroid camera mounted in the optical path was used to investigate the failure surfaces.

An Hitachi S-570 scanning electron microscope with a polaroid camera attached was used to photograph the failure surface and determine crack propagation rates.

A Leitz Miniload Hardness Tester model no. 060-366.002 serial no. 848370 was used to measure the Vickers hardness numbers.

4.2 Three Point Loading of Test Coupons

Test coupons were manufactured on a CNC lathe from 316LVM stainless steel material as shown in figure 22. All specimens were electropolished to a 2 microinch surface finish and passivated in a nitric acid solution[1]. Surface finish was measured using a Hammel Surface Roughness Tester P5-2 #D-36.1600/1985.

A three point bending apparatus was constructed as shown in Figure 23. The two reaction blocks were mounted concentrically on the circular base equidistant from the center. The semicircular form of the reaction blocks ensured the specimens were self-centering and produced a near point contact as shown in Figure 24. The diameter of the groove in the load application device was slightly larger than the minor diameter of the test coupons providing near point contact and also served to maintain alignment of the test specimens as shown in Figure 25.

All fatigue testing was conducted on an MTS Model 810 (5 Kip) servo hydraulic testing machine with function generator including waveform and frequency options, cycle counter, set point and amplitude control.

4.3 Failure Investigation of Test Coupons

The optical microscope described in 4.1 was used to investigate the failure surfaces.

The scanning electron microscope described in 4.1 was used to photograph the failure surface and determine crack propagation rates.

5 PROCEDURE

In the spring of 1988, an 18 year old male patient presented with a burst fracture of L1. He was treated by anterior decompression and stabilization with an 18 hole CASP plate and four 6.5mm cancellous bone screws. Approximately one year later, the patient presented with back pain and upon examination, two of the four screws were found to be broken. The implant was removed and obtained for failure analysis. The general procedure of failure analysis is outlined in volume 10, page 10 of the ASM Metals Handbook[7]. This procedure was followed as closely as possible except for the chemical analysis of the metal as the equipment was not available to the investigator.

5.1 Failure Investigation of Implanted Screws

Failed screws were identified on x-ray and removed from the patient. The x-rays were studied visually to determine if the relative position of the implants and bone offered any indication of the possible mode of failure. Only the head end of the screws were available for analysis as the mating surfaces were destroyed during the screw extraction process. The length of the head end of the two screws were measured and recorded in Table 1. The total length of the screws was estimated based on the number of threads seen on the preoperative x-ray and recorded in Table 1. Macroscopic

investigation was performed on both specimens while scanning electron microscope investigation was performed on one specimen.

Macroscopic investigation was performed on both specimens using a microscope. The mating fracture surfaces were photographed at different magnifications to help identify crack initiation sites, ratchet marks, beach marks, and the final fracture surface (see appendix 1.0). The thread root (parallel to the longitudinal axis) was also photographed to document where crack initiation was with respect to the thread profile (appendix 1.0).

Microscopic investigation was performed on one specimen using a scanning electron microscope. Striation spacing per cycle (da/dN) was determined at a distance 'a' from the crack initiation site (see appendix 2.0) and recorded in Table 2. The crack growth data for 316 stainless steel shown in Figure 21 was used to calculate delta K and the values were recorded in Table 2.

Vickers hardness testing was performed to determine if there were any significant variations in material properties from the screw outer surface to the inside as well as to estimate the material properties. The procedure for Vickers microhardness testing was followed according to ASTM E384. The specimens were mounted in bakelite and polished

to a suitable finish. Seventy five indentations were taken across the profile as shown in Figure 26. The raw data can be found in appendix 3.0 and the hardness number versus position across the cross section are given in Figure 27.

5.2 Analysis of Failed Implants

The fluctuating stress intensity factor (delta K) was used to calculate the alternating stress using equation 16 and the results were recorded in table 2. The maximum stress was calculated (see appendix 5.0) assuming a stress ratio of .1 and these results were recorded in Table 3. These values were used to calculate the moment required to cause these stresses using equation 8 (see appendix 5.0) and recorded in Table 3. Finally, the forces to cause these moments were determined assuming three point bending and recorded in Table 3 (see appendix 5.0).

From this analysis the average load to failure was approximately 250N which was the first load level to be applied to the test coupons.

5.3 Three Point Loading of Test Coupons

The material used for the test coupons was obtained according to ASTM-F138-82

316L grade 2-60% cold worked round bar stock of 7.9mm (.3125") as shown in Appendix 4.0. Twenty test specimens of equal major diameter (6.5mm) were fabricated on a numerically controlled lathe according to the drawings in Figure 22. Ten specimens were produced with a 3.2mm (.214") minor diameter and 2.74mm (.108") pitch. These first ten specimens were used to reproduce the failure pattern seen on the failed implants. Ten more specimens were produced with a 4.0mm (.148") minor diameter and 3.0mm(.118") pitch. These other ten specimens were used to determine the increase in cycles to failure by increasing the minor diameter.

5.3.1 3.2mm Root Diameter Test Coupons

The ten specimens with the 3.2mm root diameter were subjected to tension-tension (R=.1) fatigue testing at a frequency of 20 Hertz. The limits were set in load control with a sinusoidal wave form and a stroke limit of .5". Specimens were loaded in 3 point bending. Cycles to failure were obtained for each load level by an electromechanical counter with the results recorded in table 4 and plotted in Figure 28. Two specimens were tested at each load level to qualify scatter.

5.3.2 3.2mm Test Coupons Analysis

The nominal bending stress was calculated using equation 8 (see appendix 5.0) and recorded in table 5. The experimental maximum bending stress was calculated using equation 7 (see appendix 5.0) and recorded in Table 5. The experimental stress concentration factor was determined by dividing the experimental bending stress by the nominal bending stress (see appendix 5.0). Since the shear stress at the surface is zero, the bending stress calculated above is equal to the principal stress and the maximum shear occurs at 45 degrees from the principal direction. The maximum shear stress was determined assuming maximum shear theory (see appendix 5.0) and recorded in Table 5. The theoretical stress concentration factor (SCF) was estimated using Neuber's diagram for a circular shaft in bending as shown in Figure 29 (see appendix 5.0) and recorded in Table 6. The theoretical SCF was compared to the average experimental SCF and the results recorded in Table 6.

5.3.3 4.0mm Root Diameter Test Coupons

Procedure 4.3.1 was repeated for specimens with a 4.0mm root diameter with the results recorded in table 7 and plotted in Figure 30.

5.4 Failure Investigation of 3.2mm Root Diameter Test Coupons

Failed specimens were investigated using an optical microscope. The mating fracture surfaces were photographed at different magnifications to help identify crack initiation sites, ratchet marks, beach marks and the final fracture surface (see appendix 6.0). The thread root (perpendicular to the longitudinal axis) was also photographed to document where crack initiation was with respect to the thread profile (see appendix 6.0).

The four test coupons which showed similar failure surfaces optically to the implanted screws were investigated using a scanning electron microscope. Striation spacing was determined at a distance 'a' from the crack initiation site (see appendix 7.0) and recorded in Table 8. Crack propagation rates and stress intensity factors were calculated and recorded in table 8.

6 OBSERVATIONS AND RESULTS

6.1 Failure Investigation of Implanted Screw

X-Ray Observations

The preoperative x-ray is shown in Figure 9. The two broken screws can be seen in the upper vertebral body. The results in Table 1 show that the upper broken screw fractured approximately at its midlength. The x-ray also shows that the screw head has displaced out of the plate hole resulting in a gap at screw midlength. The two pieces have also rotated relative to one another as the longitudinal axis of two pieces are no longer aligned. It is not possible to determine if there was some additional out of plane migration of the screw from this perspective.

The lower broken screw also fractured approximately at its midlength and the resulting two pieces have displaced relative to one another as can be seen by the small increase in pitch at the fracture location. As with the upper screw, the two pieces have also rotated relative to one another.

The results in column 2 of Table 1 were measured from the fractured screws. The results in column 3 of Table 1 were estimated from the threads seen on the x-ray. The results in column 4 were calculated using the measurements taken from columns 2 and 3.

Table 1. Length of fractured screw segment and estimated total length of retrieved screws.

specimen	Length of Fractured Segment(mm)	Estimated Total Length of Screw(mm)	% Full Length
#1	17.15 (.675")	33.6 (1.323")	51
#2	22.23 (.875")	41.4 (1.631")	53

Macroscopic Observations

The light micrographs of screw #1 are shown in appendix 1.0 with magnifications varying from 8 to 40 times. Distinct semi-circular beach marks can be seen on the fracture surface in the end view direction. The cracks are centered about a common point thus locating the crack initiation site. A fissure-like mark on the fatigue surface can be seen starting around the crack initiation site area. This appears to be a ratchet mark suggesting

the possibility of multiple crack initiation sites. The side view shows the crack initiation site corresponds to the location of the smallest diameter of the thread profile. The crack propagation portion of the failure surface is approximately 90% of the total cross section. The remaining portion of the failure surface is inclined with respect to the fatigue surface.

The light micrographs of screw #2 are also shown in appendix 1.0 with magnifications varying from 17 to 40 times. There appear to be some beach marks on the crack propagation surface however they are not as well defined as those found on Screw #1. There is a distinct ratchet mark on the surface suggesting several crack initiation sites. The side view shows crack initiation from the thread root as found on Screw #1. The fatigue surface is approximately 80% of the total cross section. The final fracture zone is fibrous and is inclined to the fatigue zone plane.

Microscopic Observations

The results showed distinct striations at the two locations from the crack initiation site (appendix 2.0). The results in column 2 of Table 2 were obtained by dividing a given distance by the number of cycles over that distance (see appendix 5.0). The results in column 3 of Table 2 are the measured distance from crack initiation to the da/dN measurement site. The results in column 4 of Table 2 are the values of delta K calculated

using equations 15 and 16 (see appendix 5.0).

Table 2. Crack propagation rate and stress intensity factor at a given distance a from crack initiation for failed implants

specimen	da/dN (m/cycle E-7)	crack length a (mm)	delta K ($MPa*m^{1/2}$)
#1	4.389	0.8	20-32.04
	5.121	1.5	20-33.5

Vickers Hardness

The results of the hardness profile can be seen in Figures 26 and 27. The average hardness number was 400 which corresponds to an ultimate strength of approximately 1172MPa (170Ksi) and a yield strength of approximately 1028MPa (150Ksi)[15].

6.2 Analysis of Failed Implants

The results in column 2 of Table 3 were calculated using the results from column 4 of Table 2 (see appendix 5.0). These results were used to calculate the bending moment

(see appendix 5.0) in column 3 of Table 3. These results were used to calculate the approximate applied load (see appendix 5.0) in column 4.

Table 3. Maximum stress, bending moment and approximate load calculated from delta K in table 2.

specimen	Maximum Stress (MPa)	Bending Moment (N*m)	Approximate Load (N)
#1	590-1193	2.02-4.08	235-476
	431-911	1.47-3.12	132-280

6.3 Three Point Loading

Cycles to failure for each load level are presented in Table 4 and the graph in Figure 28. Cycles to failure increased with decreasing load as expected. The shape of the load versus log cycles illustrates the typical fatigue curve for stainless steel.

Table 4. Cycles to failure for 3.2mm root Diameter Tests Coupons

Specimen	Load (N)	Cycles to Failure	Crack Initiation From Midlength(mm)
1	250	68,720	0.36
2	250	63,540	0.91
3	200	266,190	1.54
4	200	155,680	1.17
5	275	40,290	0.74
6	275	41,170	1.04
7	150	1,000,000 DNF	-
8	175	323,620	0.91
9	175	1,235,130 DNF	-
10	162.5	1,786,980 DNF	-

The applied load in Table 4 was used to calculate the nominal bending stress in column 2 of Table 5 (see appendix 5.0). The maximum bending stress in column 3 of Table 5 was calculated using equation 7 (see appendix 5.0). The experimental stress concentration in column 4 of Table 5 was calculated using the results from columns 2 and 3 (see appendix 5.0). The maximum shear stress in column 5 of table 5 was calculated from the maximum bending stress in column 3.

Table 5. Bending stress, stress concentration factor and shear stress for 3.2mm root diameter test coupons.

	Nominal Bending Stress (MPa)	Maximum Bending Stress (Mpa)	Stress Concen-tration Factor	Maximum Shear Stress (MPa)
1	773	938	1.21	469
2	773	939	1.21	469
3	618	833	1.35	416
4	618	844	1.37	422
5	850	983	1.15	491
6	850	1035	1.22	518
7	463	-	-	-
8	540	786	1.45	393
9	540	-	-	-
10	502	-	-	-

The theoretical stress concentration factor in column 1 of Table 6 was determined using the curves in Figure 29 (see appendix 5.0). The average stress concentration factor in column 2 of Table 6 was calculated from the results in column 4 of Table 5. The percentage error was calculated from the results in columns 1 and 2 of Table 6.

Table 6. Theoretical and average stress concentration factor for 3.2mm root diameter test coupons.

Theoretical Stress Concentration Factor	Average Stress Concentration Factor from Table 5	Percentage Error
1.40	1.28	9%

Cycles to failure for each load level are presented in table 7 and the graph in Figures 30. Cycles to failure increased with decreasing load as expected. The shape of the load versus log cycles illustrates the typical fatigue curve for stainless steel.

Table 7. Cycles to failure for 4.0mm root Diameter Tests Coupons.

Specimen	Load (N)	Cycles to Failure	Crack Initiation From Midlength(mm)	Predicted Cycles to Failure
1	375	232,440	0.58	167,175
2	375	149,470	1.04	167,175
3	375	335,370	3.63	167,175
4	425	84,360	1.07	6720
5	425	97,530	0.71	6720
6	475	68,380	0.97	270
7	475	61,920	1.09	270
8	not tested	-	-	
9	350	294,210	0.84	836,125
10	350	526,930	0.84	836,125

6.4 Failure Investigation of Test Coupons

The observations made using the optical microscope showed crack initiation, propagation and fracture regions were all similar to those observed on the retrieved implants (see appendix 6.0). The size of the fatigue zone increased with decreasing load magnitude as expected.

The observations made using the scanning electron microscope showed that the fatigue striations seen on the test coupons (see appendix 7.0) were similar to those found on the retrieved implants and the reference fractographs[12].

The results in column 2 of table 8 were obtained by dividing a given distance by the number of cycles over that distance (see appendix 5.0). The results in column 3 of table 8 are the measured distance from crack initiation to the da/dN measurement site. The results in column 4 of table 8 are the values of delta K calculated using equation 26 (see appendix 5.0).

Table 8. Stress intensity factor delta K calculated from the measured crack propagation rate (da/dN) and crack length (a).

specimen	da/dN (m/cycle E-7)	crack length a (mm)	delta K ($MPa*m^{1/2}$)
#8	1.43	.337	22.6
(323,620;175N)	1.25	.789	21.8
#2	2.00	.518	22.9
(63,540;250N)	4.00	.091	31.1
	5.00	1.09	33.3
#4	2.00	.416	22.9
(155,680;200N)	2.50	.332	24.5
	2.70	.322	25.1
#3 (266,190;200N)	2.00	.185	22.9

7 DISCUSSION

7.1 Failure Investigation of Implanted Screws

X-ray Observations

The observations suggest that the screw region in contact with the bone was subjected to tensile, bending and shear loads. The tensile load was present as it maintained the position of the plate relative to the bone. The relative position of the failed screw fragments suggests there was a bending type of load. This bending was likely due to a distributed type of loading along the length of the screw with an accompanying shear load.

Sources of error included the measurement of the length of the fractured segment and the estimate of the total length of the screw from the x-ray findings.

Macroscopic Observations

The failure patterns observed in the retrieved implants were compared to those in

the reference material[7]. The failure patterns were almost identical to those for round cross sections in tension-tension and unidirectional bending fatigue with low nominal stress and a mild stress concentration. Changes in loading frequency as would be expected in-vivo probably account for the well defined beach marks. Given the relatively small contribution of the tensile stress compared to the bending stress, we can conclude that the screws failed by unidirectional bending fatigue with crack propagation across approximately 70% of the cross sectional area before fracture.

As described in section 2.1, the concave pattern of the beach marks about the crack origin may suggest a material which has a relatively lower notch sensitivity such as annealed steel. Although the author was unable to find notch sensitivity data on 316L, the ultimate tensile strength of the material used in these experiments corresponds to 316 annealed sheet with 60 % cold work[15].

The final fracture zone of both failed screws was is inclined with respect to the fatigue surface suggesting plane stress conditions.

Microscopic Observations

The striation pattern was similar to those presented in the reference books for

316L[12]. The striations found on the failed implants were not as evenly spaced as those observed on the test coupons. This may be due to the variable amplitude loading the human body is subjected to. The striations also were not as delineated as the test coupons. This may be due to post-failure surface wear associated with relative movement of the two failure surfaces prior to implant removal. Increasing the magnification of the failed implant micrographs may also have provided better results.

Sources of error included the measured length for the given number of striations used to determine the crack propagation rate da/dN as well as the distance "a"of the striations from the crack initiation site.

The results in table 2 show an increase in crack propagation rate and stress intensity factor with an increase in crack length. These results would be as expected for constant amplitude loading. However, for variable amplitude loading, this may not have been the case assuming relatively high stress magnitudes were followed by a decrease in stress magnitude.

The relation used to calculate the stress intensity factor was for 20% cold worked material as noted in section 2.4. From the graph in appendix 9.0, the ultimate tensile strength is approximately 110 Ksi for 20% cold worked. The results from the hardness

tests indicate that the ultimate strength is approximately 170Ksi which corresponds to material in a 60% cold work condition. Therefore the value of the stress intensity for material in the 60% condition will be lower. A value of 20 $MPam^{1/2}$ was assumed.

Sources of error were variations in the slope of the da/dN vs. delta K curve described above.

Vickers Hardness

The hardness results in Figure 27 show a gradual decrease in hardness from the exterior surface to the middle of the cross section. The higher hardness is probably due to local effects during the manufacturing process. The fluctuation in point to point hardness suggests that local microstructural changes are present. Given that smaller area and lower load hardness indentations are more sensitive to local microstructural changes, higher load and /or larger area hardness tests may be more representative of the materials average properties. The relatively large decrease in hardness from points 45 to 59 are not consistent with the other results. The spacing between these points on the hardness traverse is minimal and there may have been some deformation interference between indentation points. Therefore these points were neglected in the calculation of the average hardness.

As there are no markings or identifying features on the surgical screw, one cannot trace the material to a specific supplier. However, 316L has been the standard industry implant material for plates and screws for at least 10 years[1]. Given the values of the ultimate and yield strength of the material used for the test specimens, we can therefore conclude with some degree of certainty that the hardness tests are a good approximation of the material ultimate and yield strength and furthermore that the failed implant material is in fact 316L.

Sources of error in the hardness testing include the measurement of the indentation size and the indentation load calibration.

7.2 Analysis of Failed Implants

The assumption of LEFM was investigated and the results given in appendix 5.2. The plastic zone size was calculated from the yield strength and the fluctuating stress intensity factor using equation 25. The plastic zone size and the implant thickness were substituted into equation 24 and the results indicated that the assumption of LEFM is valid.

Although bending was argued to be the dominant load pattern for the failed

implants, the presence of other loads may affect the results obtained using this equation. It should be noted that the value for the diameter of the shaft was the effective diameter based on the tensile stress area of the thread. The results for a beam with a circular arc crack provide more reasonable results given the load levels obtained for the test coupons. All of the results depend on the value for da/dN obtained from the micrographs.

The bending stress in table 3 was also calculated using the effective diameter of the thread. As noted in section 2.5, the formula presented in this section were developed for 60 degree symmetrical threads or "V" form. The tensile stress area used for stress calculations is based on the average between the pitch and the minor diameter. The thread profile of the surgical screws is non-linear of constant radius from crest to root and is non-symmetrical. When the tensile area of the surgical screws is calculated using the equations for the symmetrical threads, the resulting effective diameter is not equal to the average of the pitch and the minor diameters as expected. However, this value of the effective diameter provides reasonable results in estimating the stress concentration factor in table 5. If one chooses the value for the effective diameter equal to the mean of the pitch and minor diameters, the stress concentration factors in table 5 would be less than 1.0.

The approximate load in column 4 of table 3 are within the loads reported to be

transmitted through the spine column[20]. The range of values varies greatly depending on such factors as body weight, muscle condition and activity level.

7.3 Three Point Loading

A simply supported member subjected to three point bending results in the bending moment being maximum at the midlength of the beam. Therefore this experimental load pattern was chosen to attempt to ensure failure at the same point for all specimens. The general design of the test specimens was modeled after specimens found in the reference material[2]. The specimens shown in Figures 22 were originally designed to be identical except for the minor diameter. Errors introduced in the production of the prototypes resulted in additional differences between the two different sizes of specimen. The errors introduced in the 4.0mm minor diameter specimens were (i) the distances between each end of the specimen and the reaction groove are not equal, (ii) the slope of both chamfers are not identical. However, the distance between the reaction point grooves is identical (6.35cm=2.5").

When the specimens were positioned in the test fixture, the load application device was in contact with the minor diameter midway between threads. This was done so as to approximate a point load. Directly on the opposite side of the load application device, was

the full thread diameter. Therefore it was not possible for a crack to initiate at the exact midlength of the specimen. The results in column 4 of table 4 and column 4 of Table 7 indicate the distance the crack initiation was from the midlength of the specimen. Any errors in misalignment during the positioning of the specimen would increase this deviation.

7.3.1 3.2mm Root Diameter Test Coupons

The results in Table 4 showed for increasing load, there was a corresponding decrease in cycles to failure as expected. The specimens loaded at 275 and 250 N showed little scatter. The other load levels showed considerable scatter with scatter increasing with decreasing load. These results are typical of fatigue test data as described in section 2.3.5. The P-N curve in Figure 28 is approximately linear as expected. Although the data is normally presented in terms of stress, given that the exact stress area is not known, the data was left in terms of load.

When a simply supported member is loaded, the deflection causes a change in span length. The load and deflection therefore are no longer proportional to each other[25]. The change in length or test coupon elongation (TCE) was calculated in appendix 5.0. The results indicate that the TCE is negligible compared to the overall length.

Sources of error included (i) the machining of all the apparatus components which affected the alignment of the specimens, (ii) the machining and finishing of the test coupons (iii) the position of the reaction blocks with respect to the center of load application device, (iv) small fluctuations in hydraulic line pressure, and (v) small changes in load amplitude voltage settings.

7.3.2 3.2mm Test Coupons Analysis

The maximum bending stress results in Table 5 were calculated for each of the specimens which failed. All of these values were above the estimated endurance limit of the material (731MPa). Specimens 7 and 10 were below the endurance limit if one assumes a stress concentration factor of 1.4. As specimens 8 and 9 were tested at the same load level, other factors besides the load level contributed to failure of specimen 8. Microscopic surface defects or errors during the positioning procedure may have contributed to differences in the results of these two load levels. The moment arm was taken to be the midlength of the specimen.

The theoretical stress concentration factor in Table 6 is only an approximation since the thread profile is not a symmetrical groove as shown in Figure 29. The radius chosen for the groove was .75mm which is the smaller of the two radii. The theoretical

value is greater than the experimental stress concentration factor as expected. This is due primarily to the mutual relief afforded by adjacent threads.

7.3.3 4.0mm Root Diameter Test Coupons

The results in Table 7 showed for increasing load, there was a corresponding decrease in cycles to failure as expected. The specimens loaded at 425 and 475 N showed little scatter. The other load levels showed considerable scatter with scatter increasing with decreasing load. These results are typical of fatigue test data as described in section 2.3.5. The P-N curve in Figure 30 is approximately linear as expected. As with the 3.2mm specimens, the data was left in terms of load. Comparing the P-N curves for the 3.2mm and 4.0mm specimens, one can see that the fatigue strength of the 4.0mm specimens is higher as expected. The TCE was calculated for these tests as well and the results indicate that the TCE is negligible compared to the overall length.

The equations used to estimate the stress concentration factor for the 3.2mm specimens were rearranged to try to predict the cycles to failure for the 4.0mm specimens. This did not provide consistent results. The first problem encountered was in the estimate of the effective diameter of the thread. Following the same procedure as for the 3.2mm specimens resulted in an effective diameter of 3.85mm which is obviously incorrect since

this will always be larger than the minor diameter of the thread. The minor diameter was then estimated by solving for the same ratio for the 4.0mm as for the 3.2mm resulting in an effective diameter of 4.68mm. The predicted results in column 5 of Table 7 were reasonable for the lower load/higher cycle failures than for the high load/low cycle failures. Another contributing factor in attempting to predict cycles to failure is the amount of scatter typically found in the fatigue testing of identical specimens.

7.4 Failure Investigation of Test Coupons

Macroscopic Observations

The fatigue patterns seen on the light micrographs were similar to the ones observed on the failed implants with the noticeable absence of beach marks. As described in section 2.1, beach marks are generally not observed in laboratory tests under constant amplitude loading. Multiple crack initiation sites can be seen on some of the specimens however, there are no distinct ratchet marks as seen on the failed implants. The fatigue zones are smooth and distinct. The final fracture zones are distinctly fibrous and in the same plane as the fatigue zone thus suggesting plane strain conditions.

Microscopic Observations

The striation patterns seen on the test specimens were well delineated and evenly spaced over the measurement length. These striations were much easier to identify than the striations for the failed implants. Apart from the reasons stated above, the distinctiveness of the striations may in part be due to the higher magnifications employed for these measurements.

The crack propagation rates in Table 8 were approximately half the value of those obtained for the failed implant and thus the stress intensity factors were also lower than average. However, the stress intensity factors were within the range presented in Table 1. These results suggest that the three point bend test produced a stress field ahead of the crack tip that was representative of the stress field produced in-vivo.

8 CONCLUSIONS

From the forgoing discussion, we may conclude that the failure mode was uniaxial bending with some additional tensile and shear loads. As the fracture surfaces were almost identical and the crack propagation rates were of the same order of magnitude, three point bending provides a reasonable approximation of the stress state in-vivo and thus is a useful method for testing future designs. The validity of the model was partially supported by the increase in cycles to failure for increasing cross section (4.0mm minor diameter threads). Although the prediction of cycles to failure for 4.0mm minor diameter threads was not consistent for all load levels, this can in part be attributed to the lack of knowledge as to the stress concentration and the tensile area of the thread profile and the inherent scatter of fatigue testing.

9 RECOMMENDATIONS

The following recommendations would help to improve the results obtained in this study ;

- more rigorous investigation of the failed implant surfaces including both hardness profiles and scanning electron micrographs to determine the variation in crack growth rate across the cross section ; this may also contribute to the establishment of a loading spectrum for loading in the spine,

- numerical analysis of thread profile would improve the approximation of the stress concentration factor and tensile area of the thread profiles,

- increasing the smaller of the two radii of the thread profile would decrease the stress concentration at this point

- ideally a load spectrum needs to be developed to more closely represent the load pattern in the human body at different locations.

- failure investigaton of further implant failures should be performed so that a data base

can be established to look for common features which may suggest other design improvements

In attempting to make recommendations from the results of this investigation, one must recall that the loading patterns vary greatly from patient to patient and depend on many factors. Thus the failure mode observed in one patient may not necessarily be the same failure mode observed in another.

10 REFERENCES

1. Annual Book of ASTM Standards, Volume 13.01, Medical Devices, American Society For Testing and Materials, Philadelphia, 1991, p27.

2. Annual Book of ASTM Standards, Volume 03.01, "A370-77 Standard Method and Definitions for Mechanical Testing of Steel Products", Metals Test Methods and Analytical Procedures, American Society For Testing and Materials, Philadelphia, 1986.

3. Annual Book of ASTM Standards, Volume 03.01, "E384-84 Standard Test Method for Microhardness of Materials", Metals Test Methods and Analytical Procedures, American Society For Testing and Materials, Philadelphia, 1986.

4. Barsom, J.M. and Rolfe, S.T. `Fracture and Fatigue Control in Structures`.Prentice Hall, Englewood Cliffs, New Jersey, 1987.

5. Black, R.C., Gardner, V., O'Neil, J., Armstrong, G.W.D., St. George, M., 'A Contoured Anterior Spine Plate', Clinical Orthopaedics and Related Research, #227;153, 1988.

6. Boresi, Sidebottom, Seely, Smith, 'Advanced Mechanics of Materials', third edition, John Wiley and Sons, New York, 1978

7. Boyer, H.E. Metals Handbook, Vol. 10, 8th edition, American Society for Metals, Metals Park, Ohio, 1975.

8. Boyer, H.E. Metals Handbook, Vol. 10, 9th edition, American Society for Metals, Metals Park, Ohio, 1986.

9. Bundy, K.J., Desai, V.H.,'Studies of SCC behavior of Surgical Implant Materials Using a Fracture Mechanics Approach', ASTM STP 859, 1985, pp.73-90.

10. Chow, D., Armstrong, G.W.D., 'The First 25 Cases of the Contoured Anterior Spine Plate' in Proceedings of the Annual Meeting of the Scoliosis Research Society, Honolulu, Hawaii, 1990.

11. ESDU "Crack Propagation, Stress and Strength Sub Series ; 80036", Volume 7, Engineering Science Data Unit, London, U.K., 1980.

12. Fellows, J.A., Metals Handbook, Vol. 9, 8th edition, American Society for Metals, Metals Park, Ohio, 1975.

13. Gilbert, S.G. "A Pilot Study to Investigate Screw Behaviour in Anterior Spinal Fixation", in Proceedings of the 13th Annual Meeting of the Canadian Medical and Biological Engineering Society, Halifax, Nova Scotia, 1987, pp 39-40.

14. Gilbertson, L.N., "Stress Corrosion Cracking of 316LVM" in the proceedings of the 4th Annual Meeting of the Society of Biomaterials.

15. Ho, C.Y., "Aerospace Structural Metals Handbook", Volume 2, U.S.A.F., CINDAS/Purdue University, Indiana, 1992.

16. Murakami, Y., "Stress Intensity Factors Handbook", Japanese Society of Material Science, Volume 2, Permagon Press, 1986.

17. Oborg, E., Jones, F.D., Horton, H.L., "Machinery's Handbook" 20th edition, Industrial Press, N.Y., 1976.

18. Peterson, R.E., 'Stress Concentration Factors For Design', Wiley, New York, 1974.

19. Pohler, O.E.M., "Morphological and Electrochemical Studies of Fatigue and Corrosion Fatigue of Three Orthopaedic Implant Materials",in Proceedings of the Society of Biomaterials 10th Annual Meeting, pg. 122, 1984.

20. Schultz, A.B., "A Mathematical Model for the Study of the Mechanics of the Human Vertebral Column", J. Biomechanics, Vol. 3, pp405-416, 1970.

21. Schutz, W.,"Standardized Stress-Time Histories-An Overview", Development of Fatigue Spectra, ASTM STP 1006, American Society for Testing and Materials, Philadelphia, 1989, pp. 3-16.

22. Sheenan, J.P., Morin, C.R.,.Packer, K.F. 'Study of SCC Susceptability of Type 316L Stainless Steel In-Vivo' ASTM STP 859, 1985, pp. 57-72.

23. Shigley, J.E.,"Mechanical Engineering Design", 3rd edition, McGraw Hill, 1977.

24. Sih, G.C., Handbook of Stress Intensity Factors for Reserachers and Engineers, Institute of Fracture and Solid Mechanics, Lehigh University, Bethlehem, Pa., 1973.

25. Spotts, M.F. Design of Machine Elements, 6th edition, Prentice Hall, New Jersey, 1985.

26. Van Vlack, L.H., "Elements of Materials Science and Engineering, Fourth Edition, Addison Wesley, 1980.

27. Vert, M., Christel, P., Chabot, F., Leray, J., "Bioresorable Plastic Materials for Bone Surgery" in Macromolecular Biomaterials

28. Wulpi, D.J., "How Components Fail", American Society for Metals, 1966.

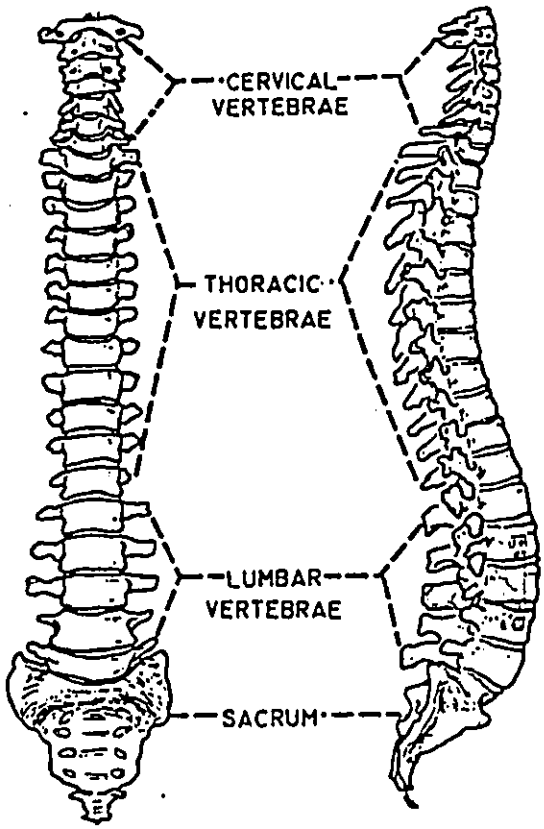

Figure 1. Regions of Human Spine[20]

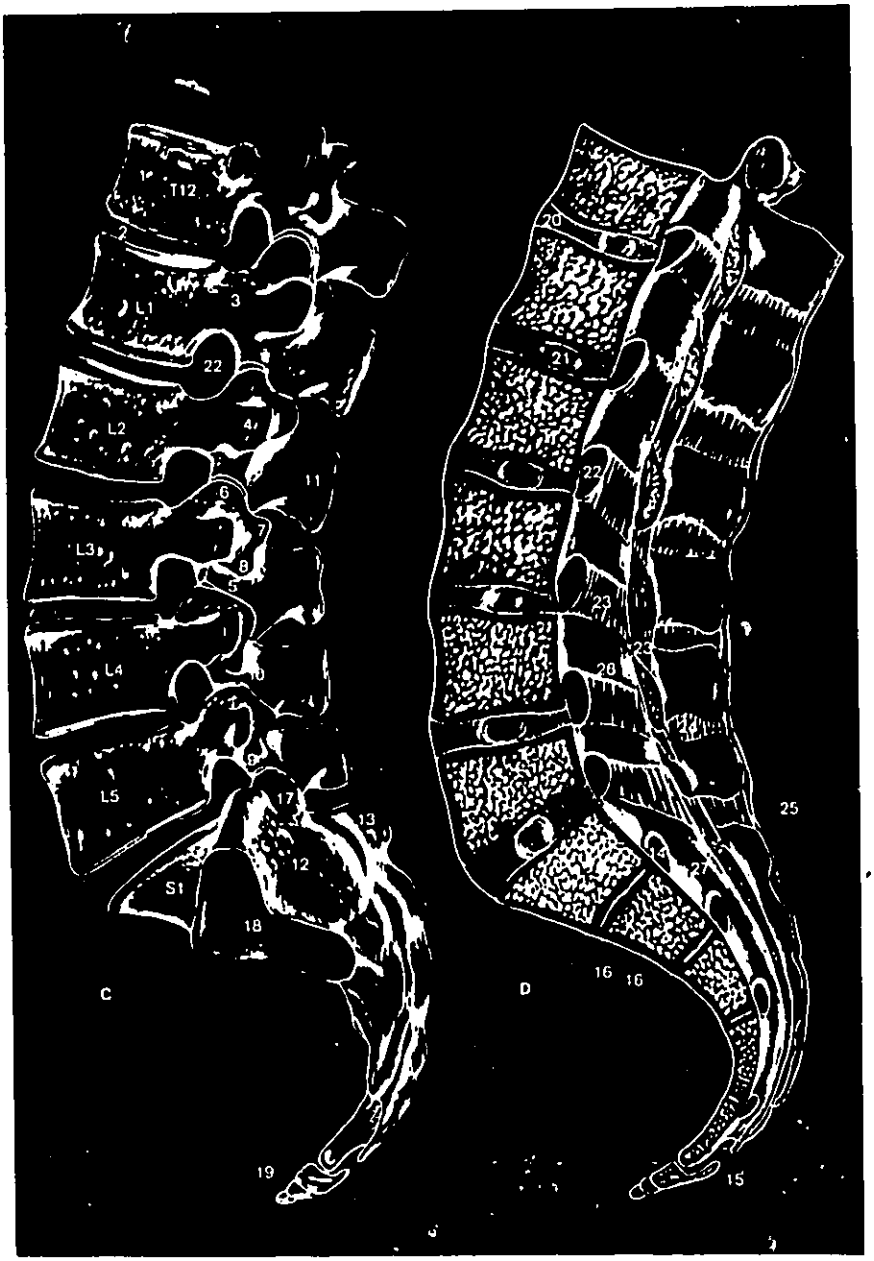

Figure 2. Lumbar Spine[20]

Figure 3 CT scan of normal vertebrae showing triangular shape of the spinal canal

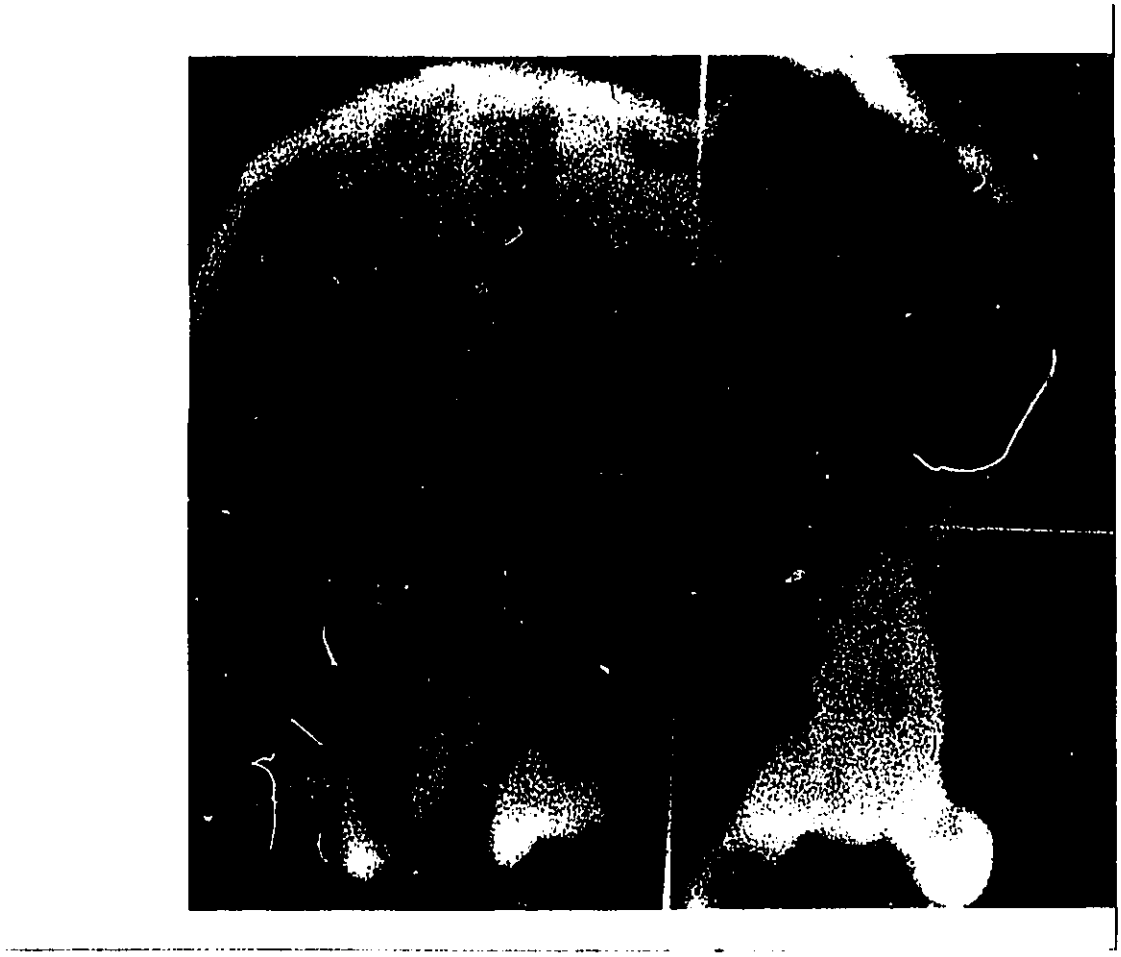

Figure 4. CT scan of fractured vertebrae with bone fragments in spinal canal

Figure 5. Various plate sizes from the CASP system

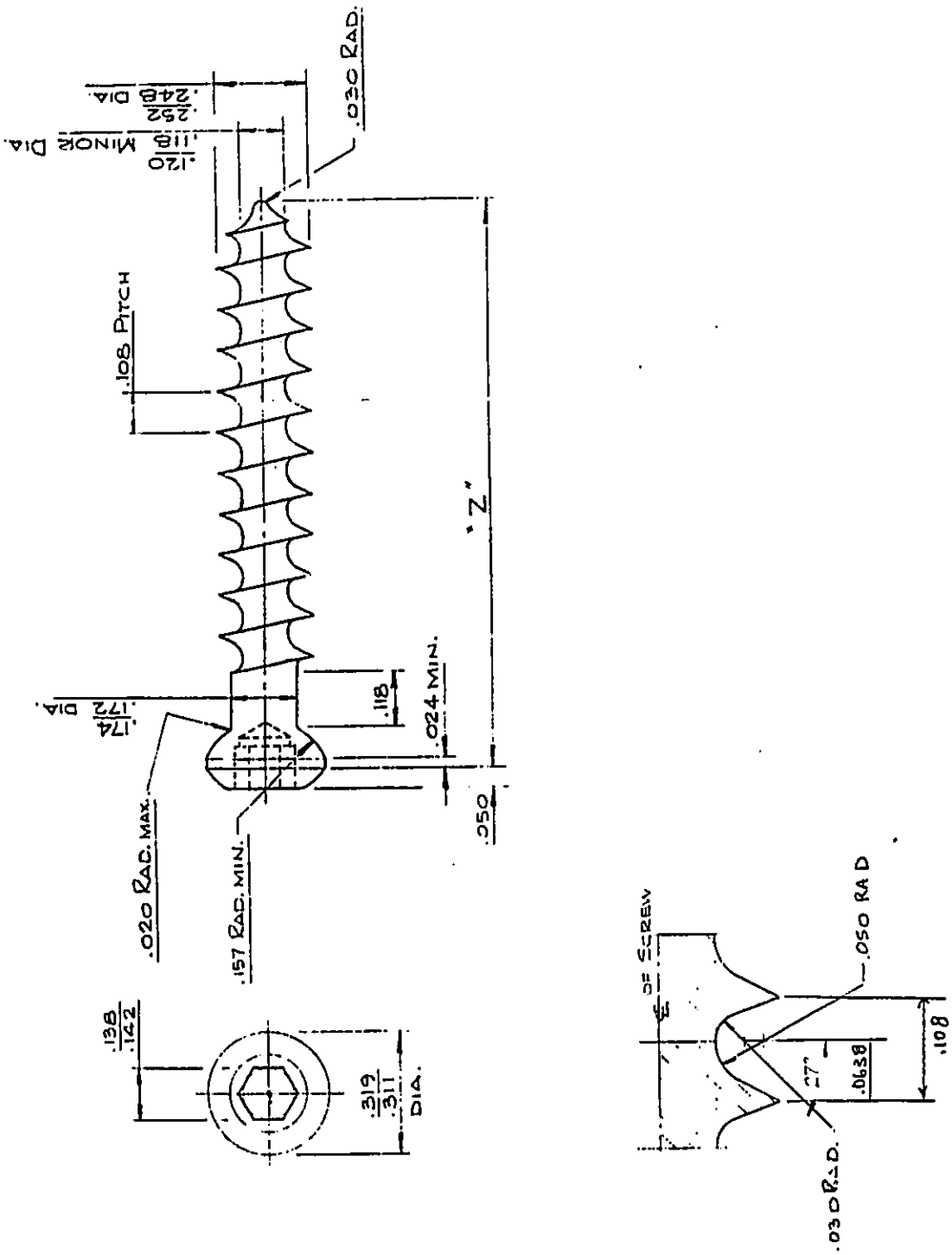

Figure 6. Cancellous bone screw

Figure 7. Model of surgical construct.

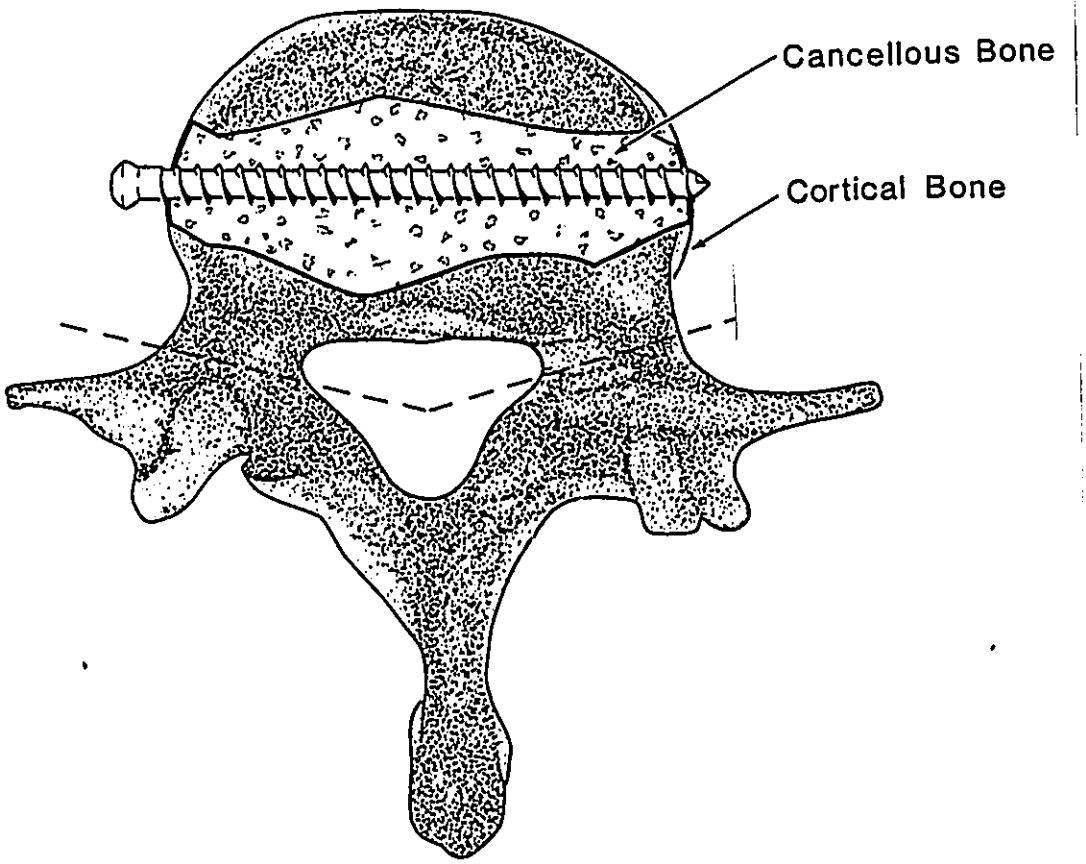

Figure 8. Full width engagement of screw in vertebrae

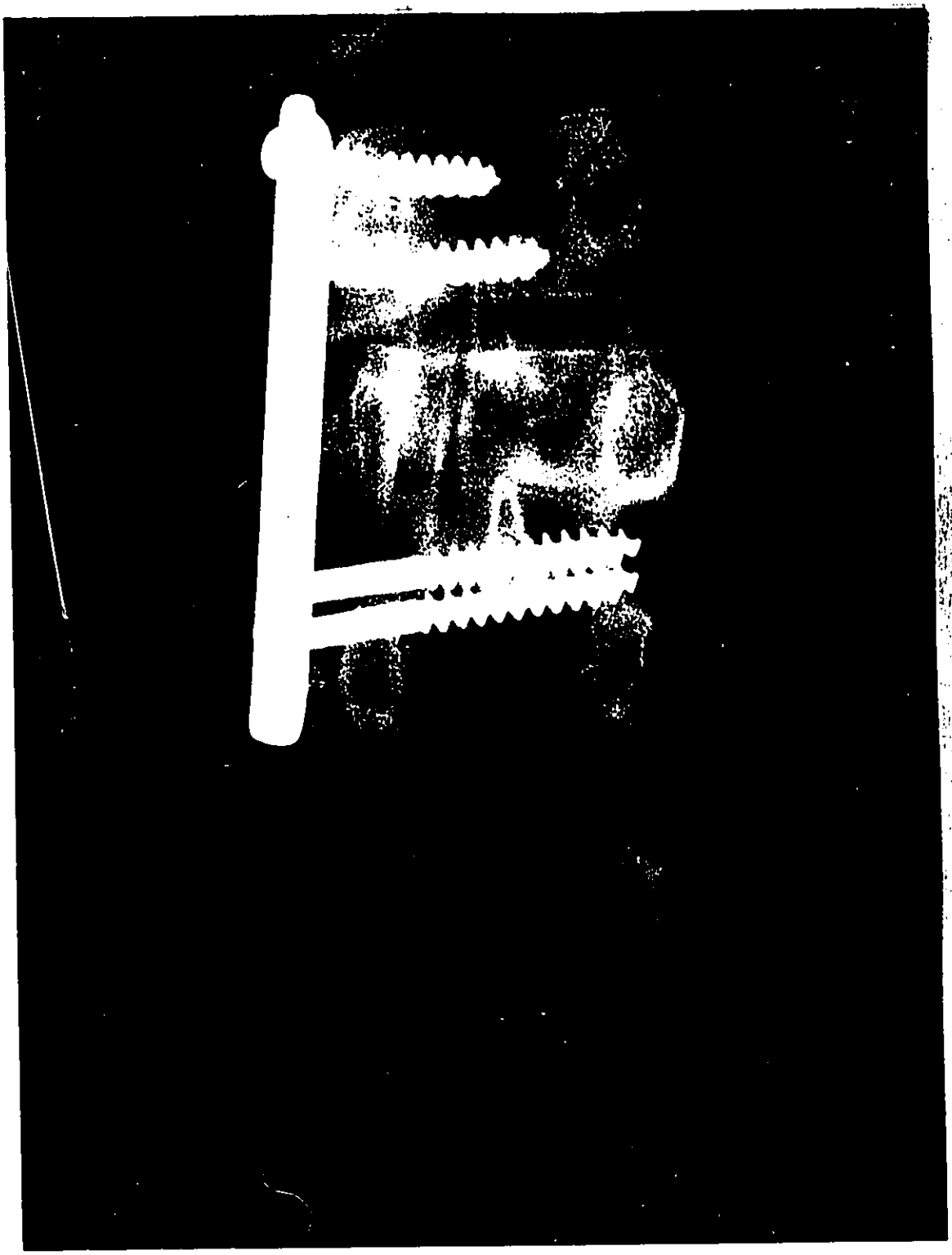

Figure 9 X-ray showing broken screws in-vivo.

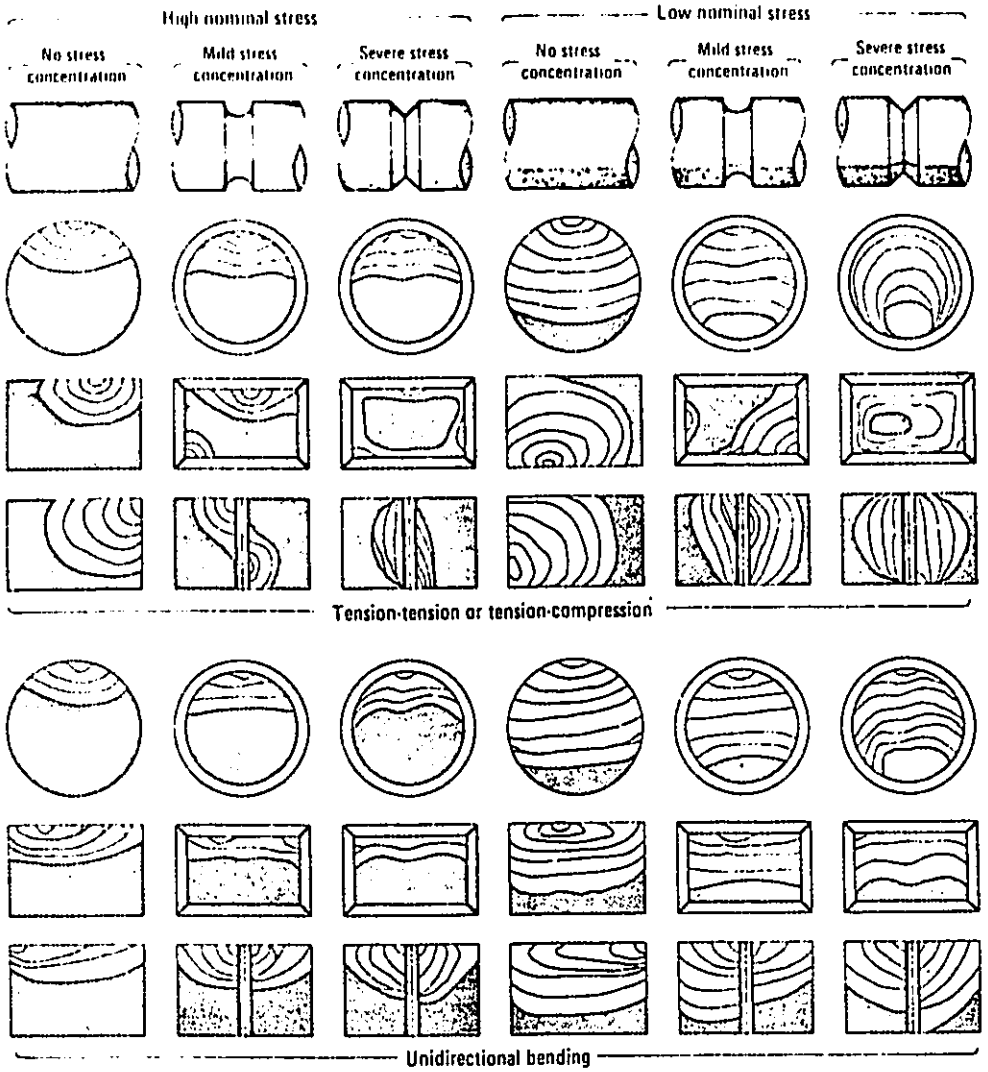

Figure 10. Typical beach marks seen on a round shaft subjected to various load levels, stress concentrations and loading patterns[7].

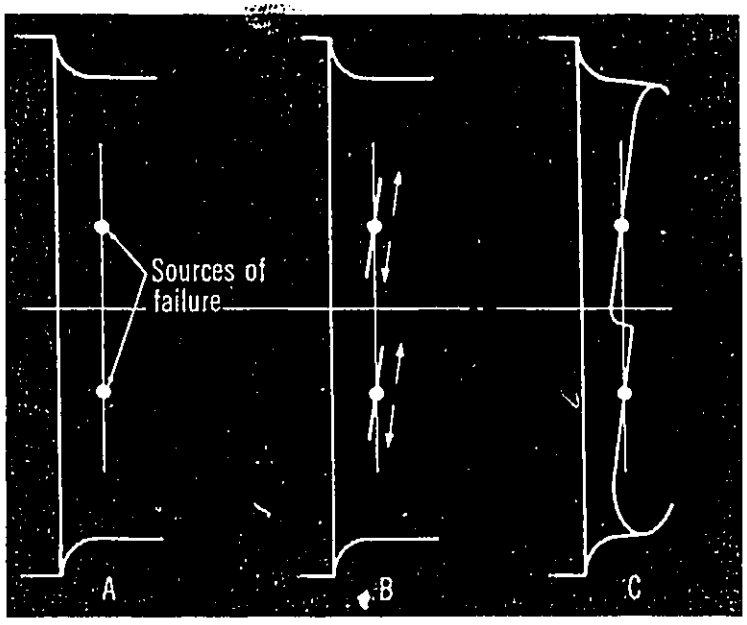

Figure 11. Typical progression of crack initiation and progression during the formation of ratchet marks[28].

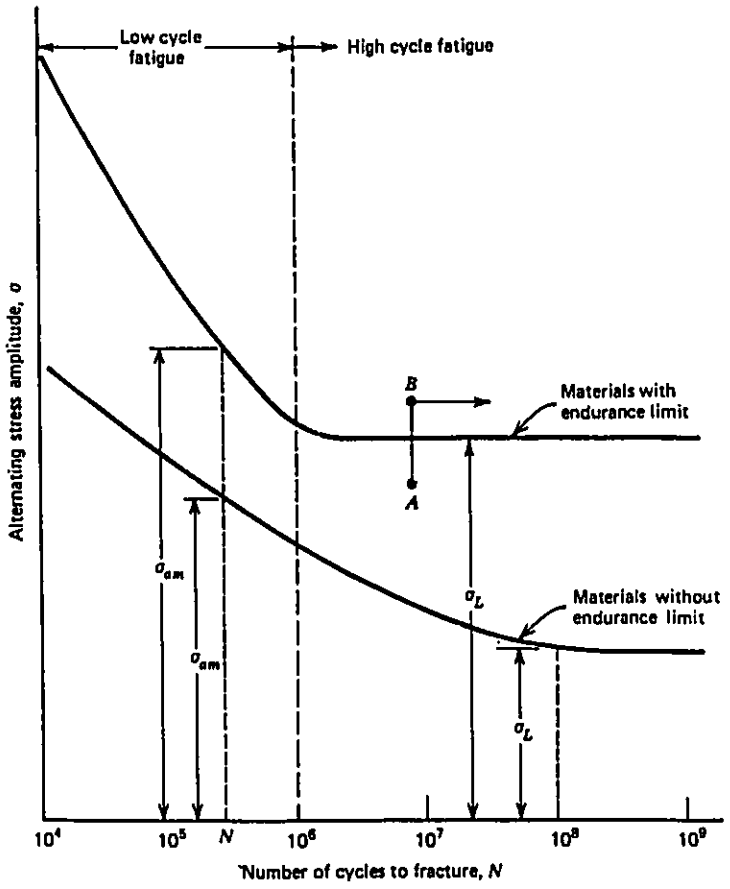

Figure 12. Typical SN curve showing endurance limit[6].

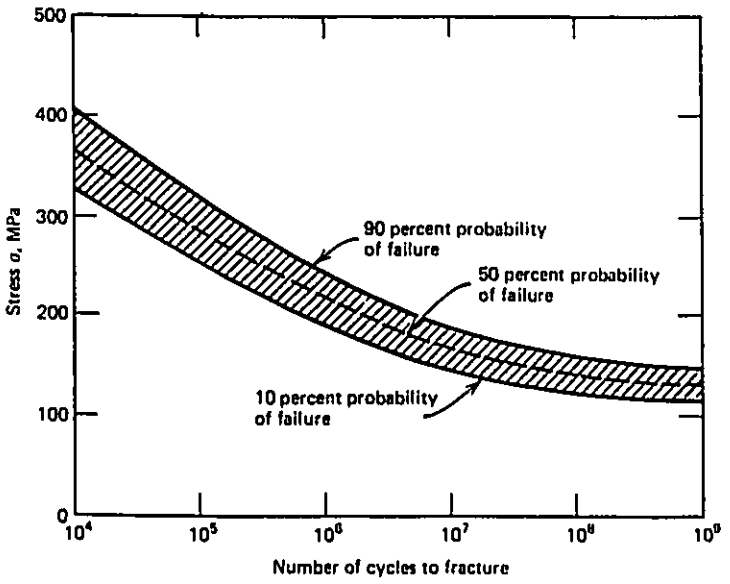

Figure 13 SN probability failure band[6].

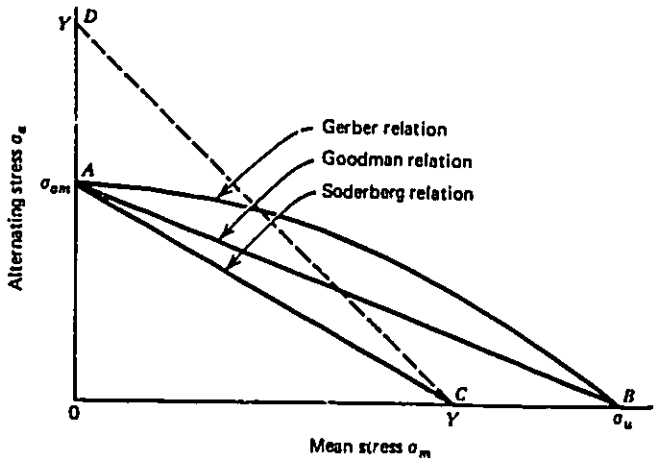

Figure 14. Alternating stress versus mean stress[6].

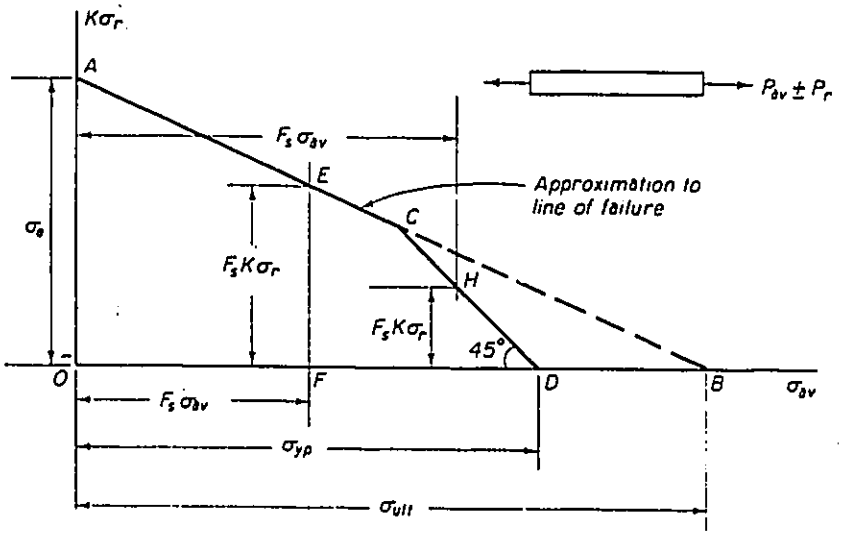

Figure 15 Modified Goodman diagram[25].

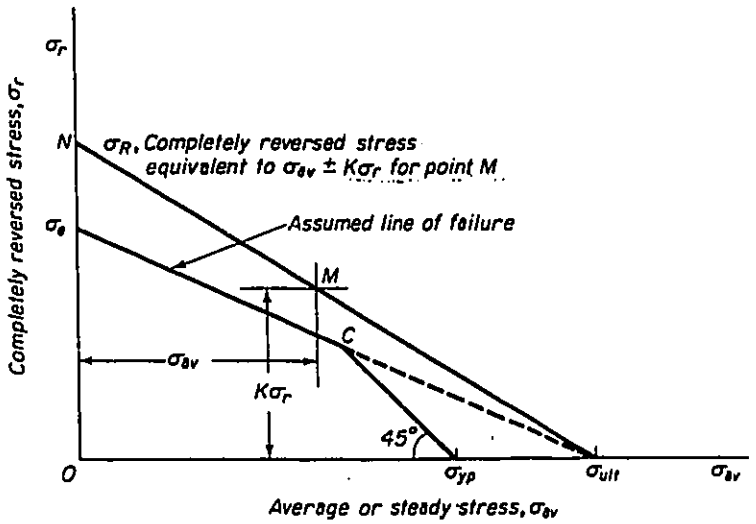

Figure 16 Completely reversed stress versus average stress[25].

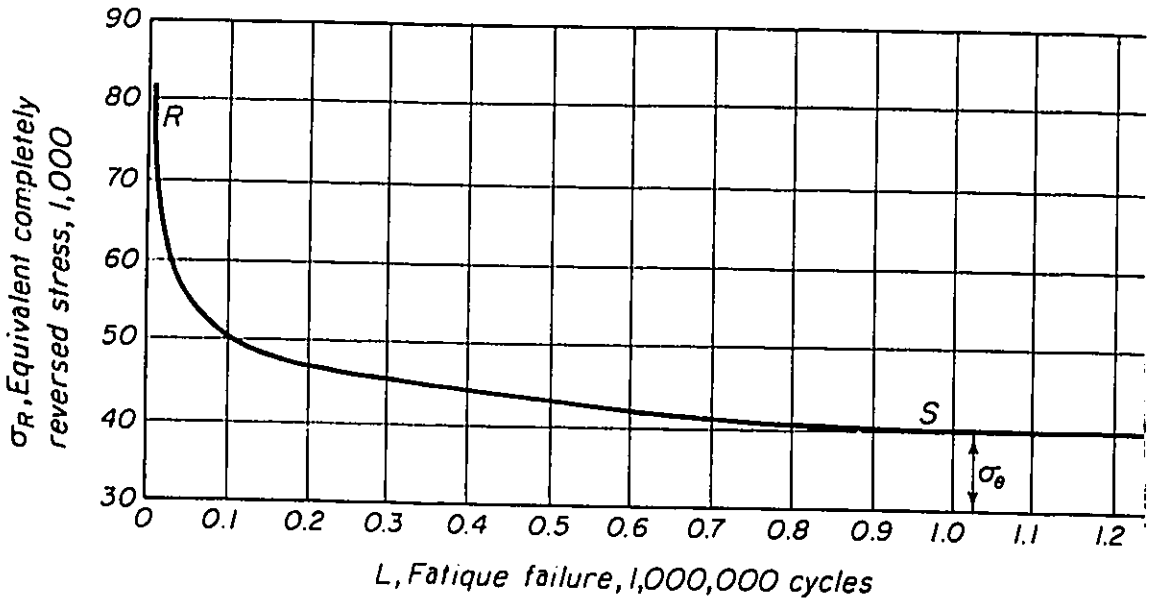

Figure 17 Equivalent completely reversed stress versus cycles showing endurance limit[25].

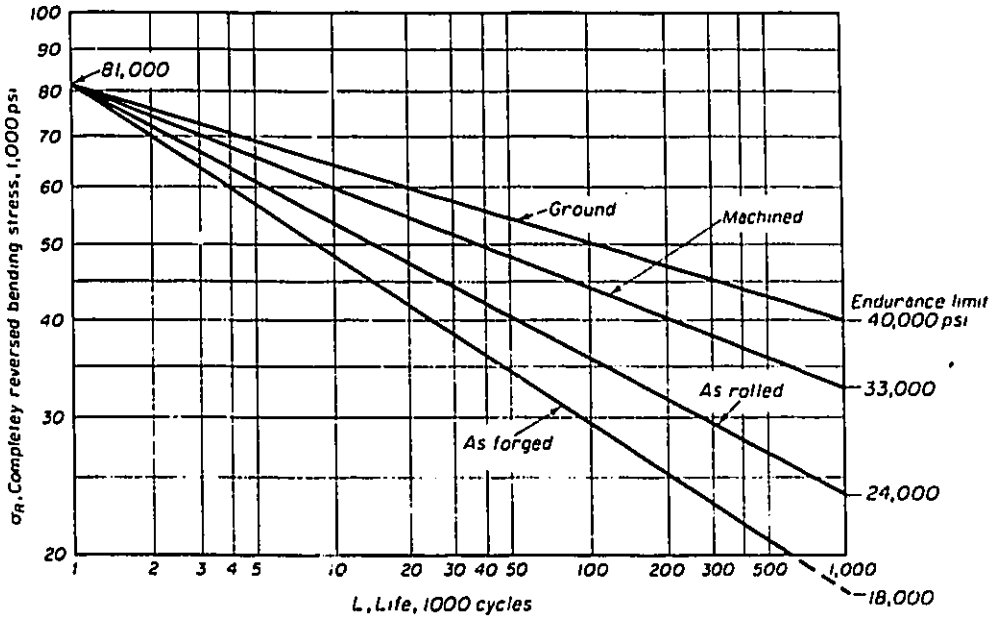

Figure 18 Typical failure curve of reversed stress versus cylces[25]

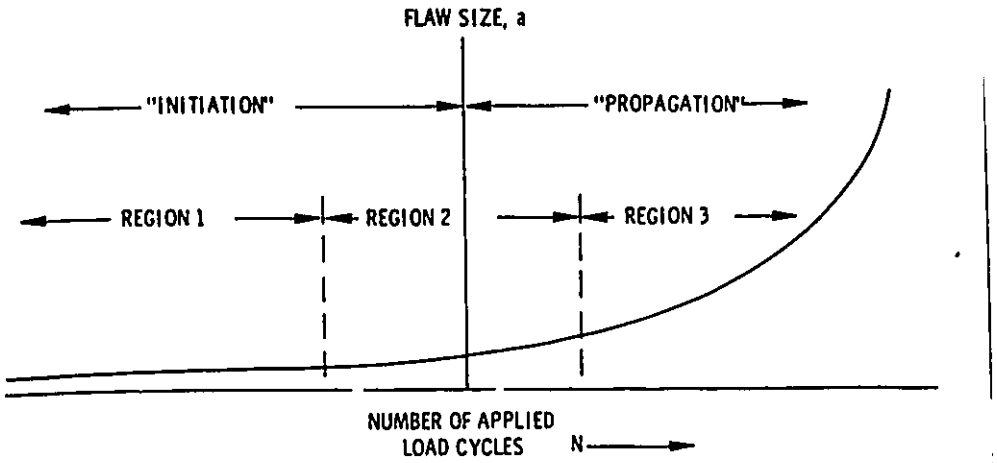

Figure 19 Flaw size versus cycles[4].

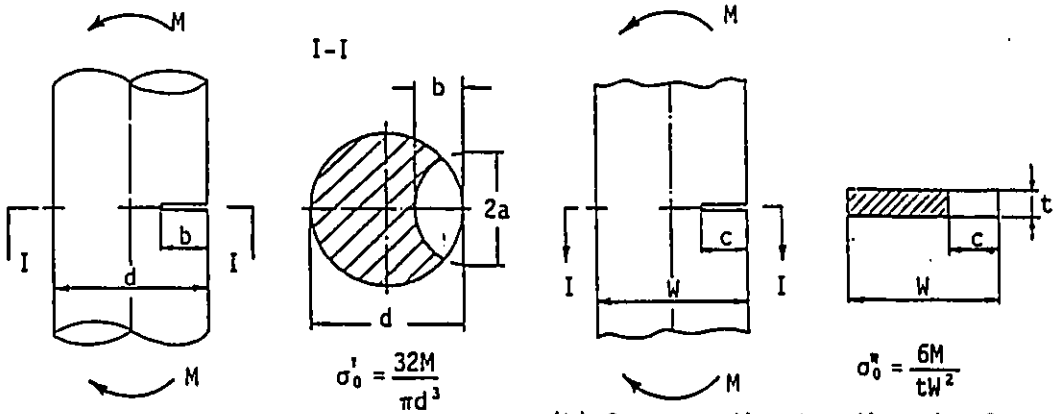

Figure 20 Semi-ellipitical crack in a shaft under bending[24].

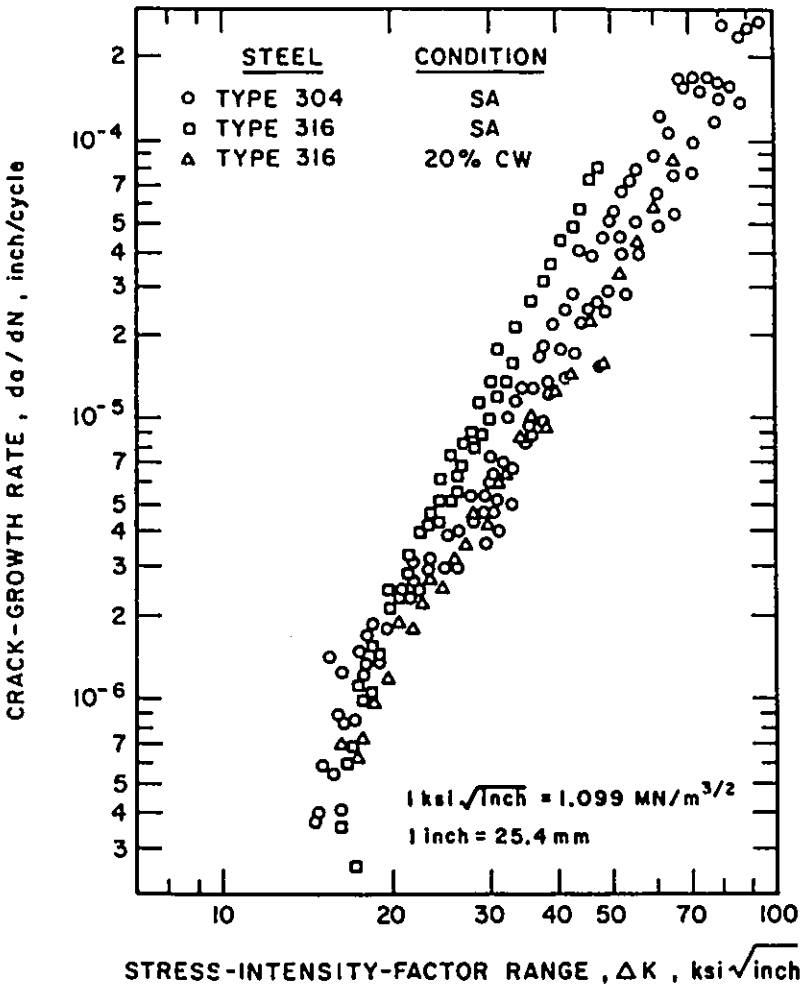

Figure 21 Crack growth rate versus stress intensity factor[6].

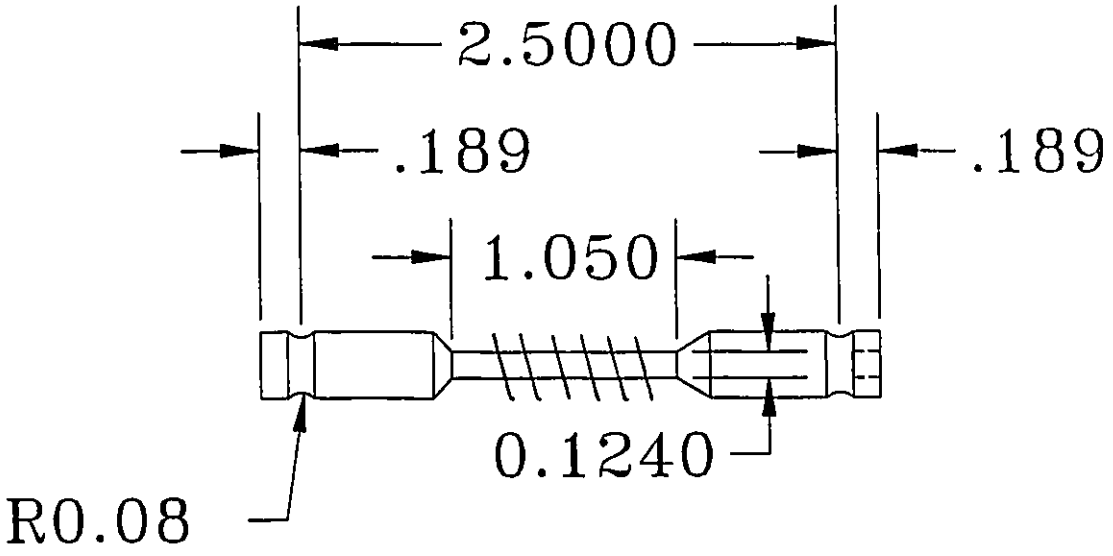

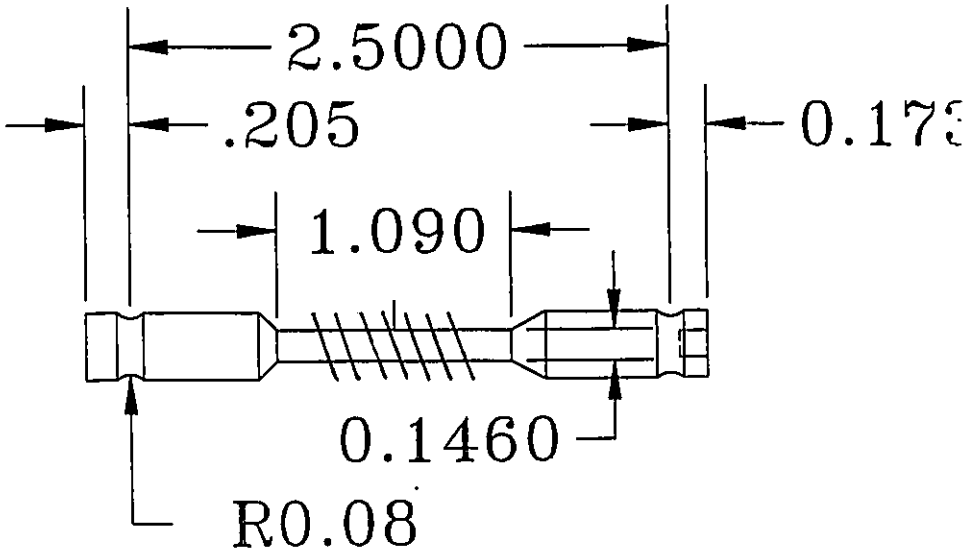

Figure 22 Test coupons fabricated for three point bending tests

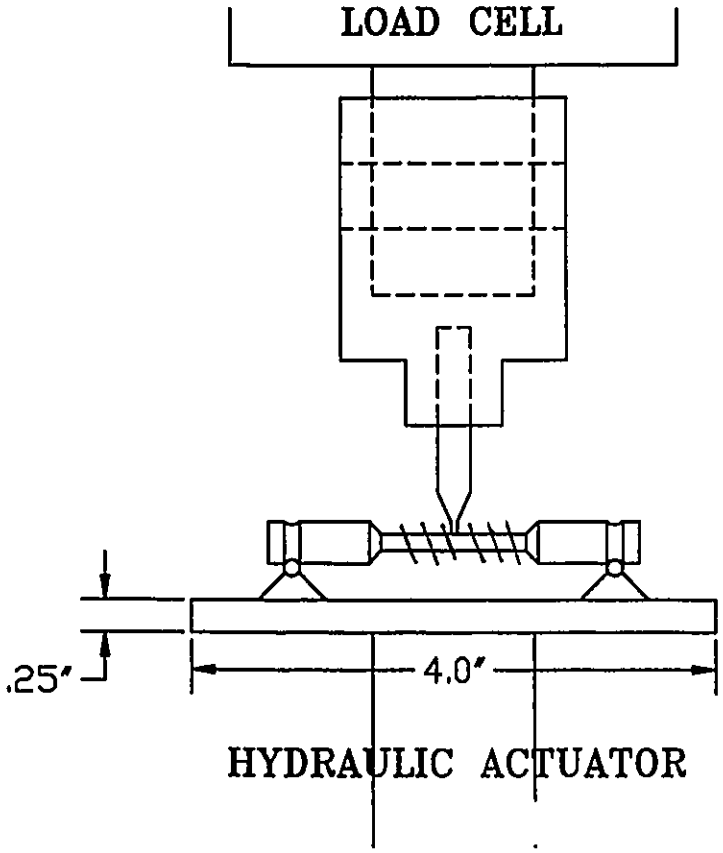

Figure 23 Three point bend apparatus

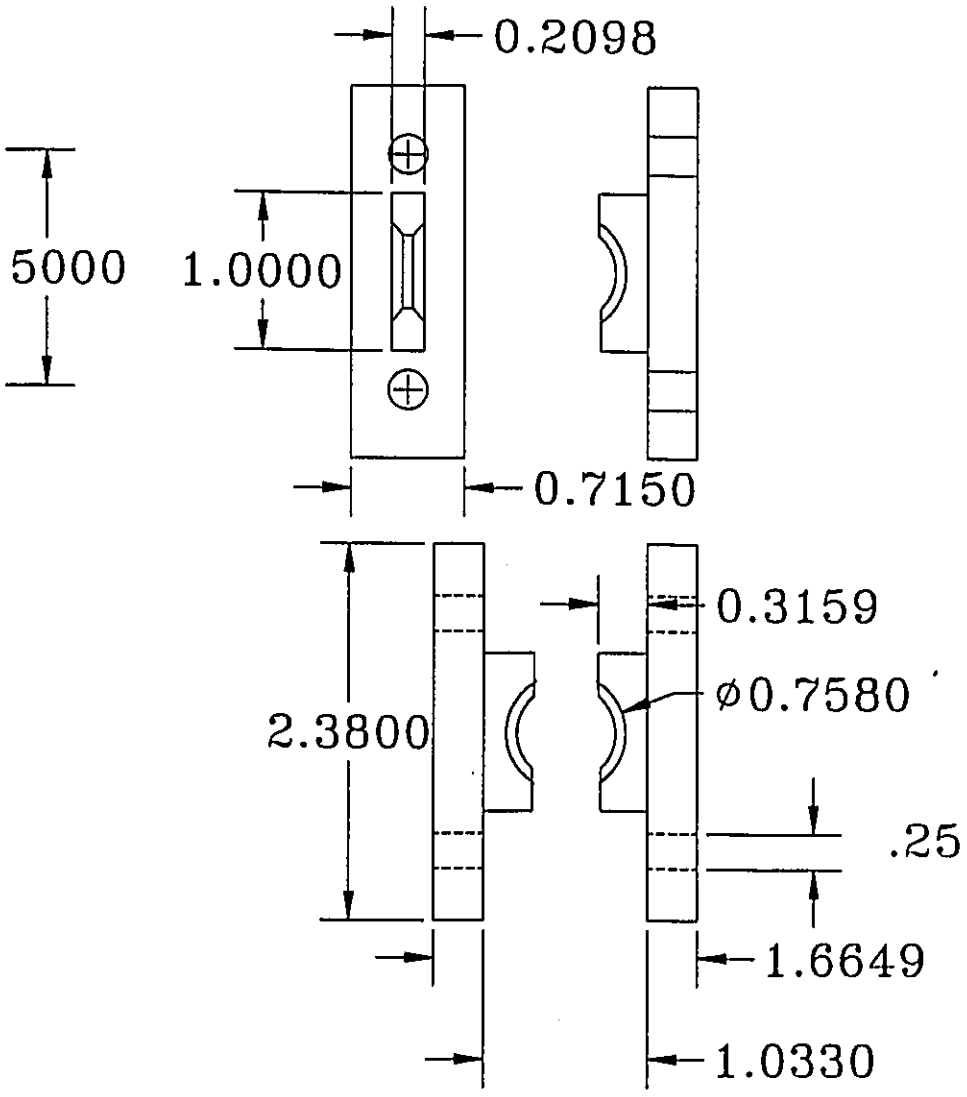

Figure 24 Reaction blocks for three point bending apparatus

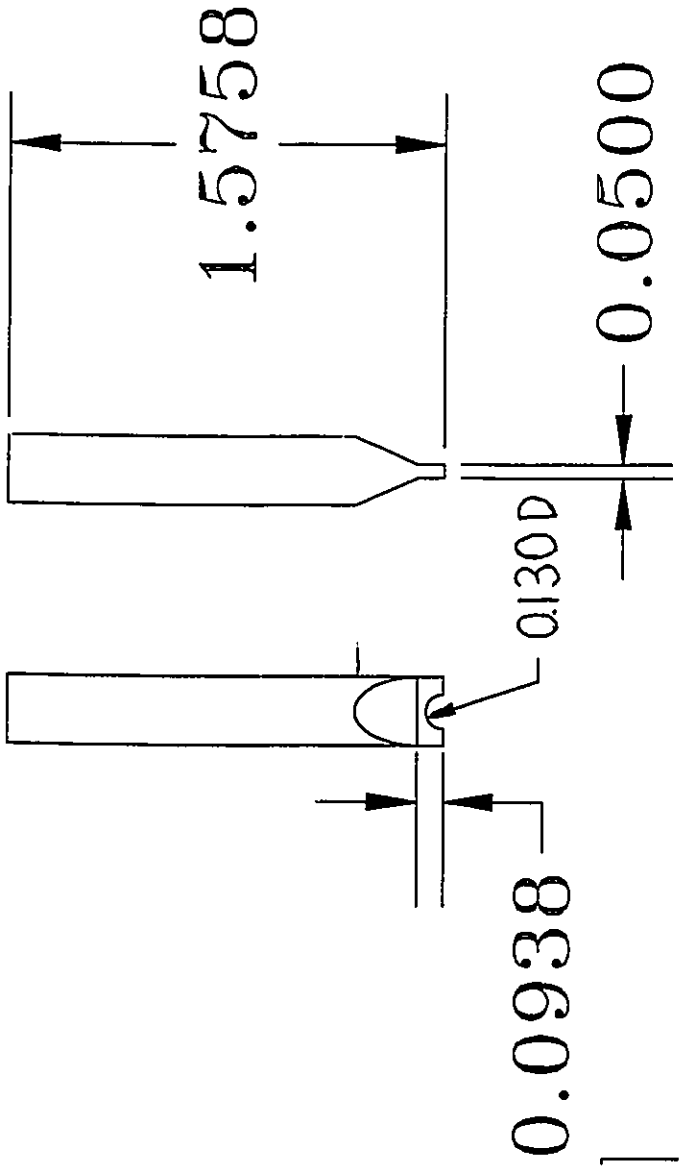

Figure 25. Load application device.

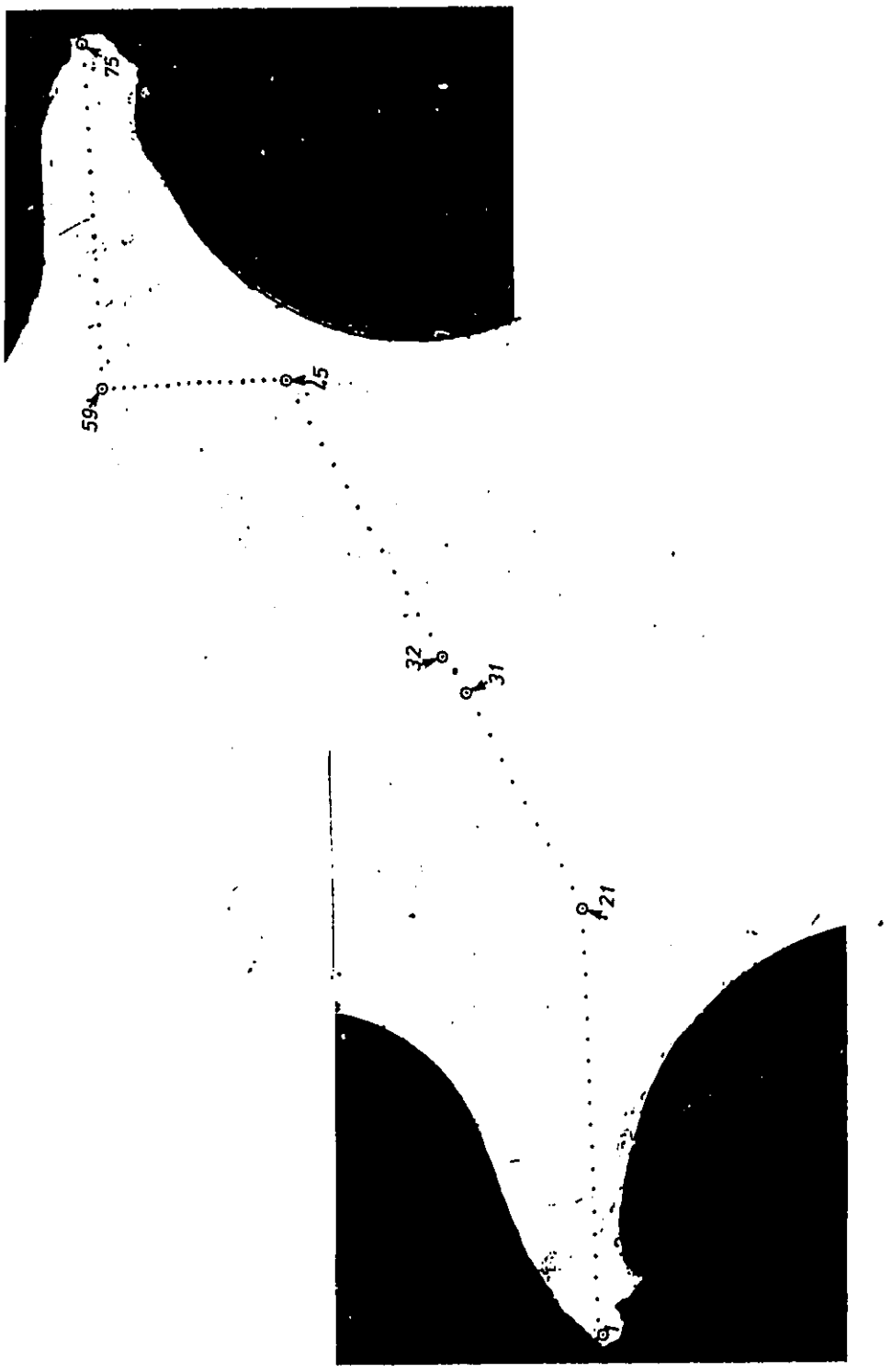

Figure 26 Vickers hardness traverse on failed implant cross section.

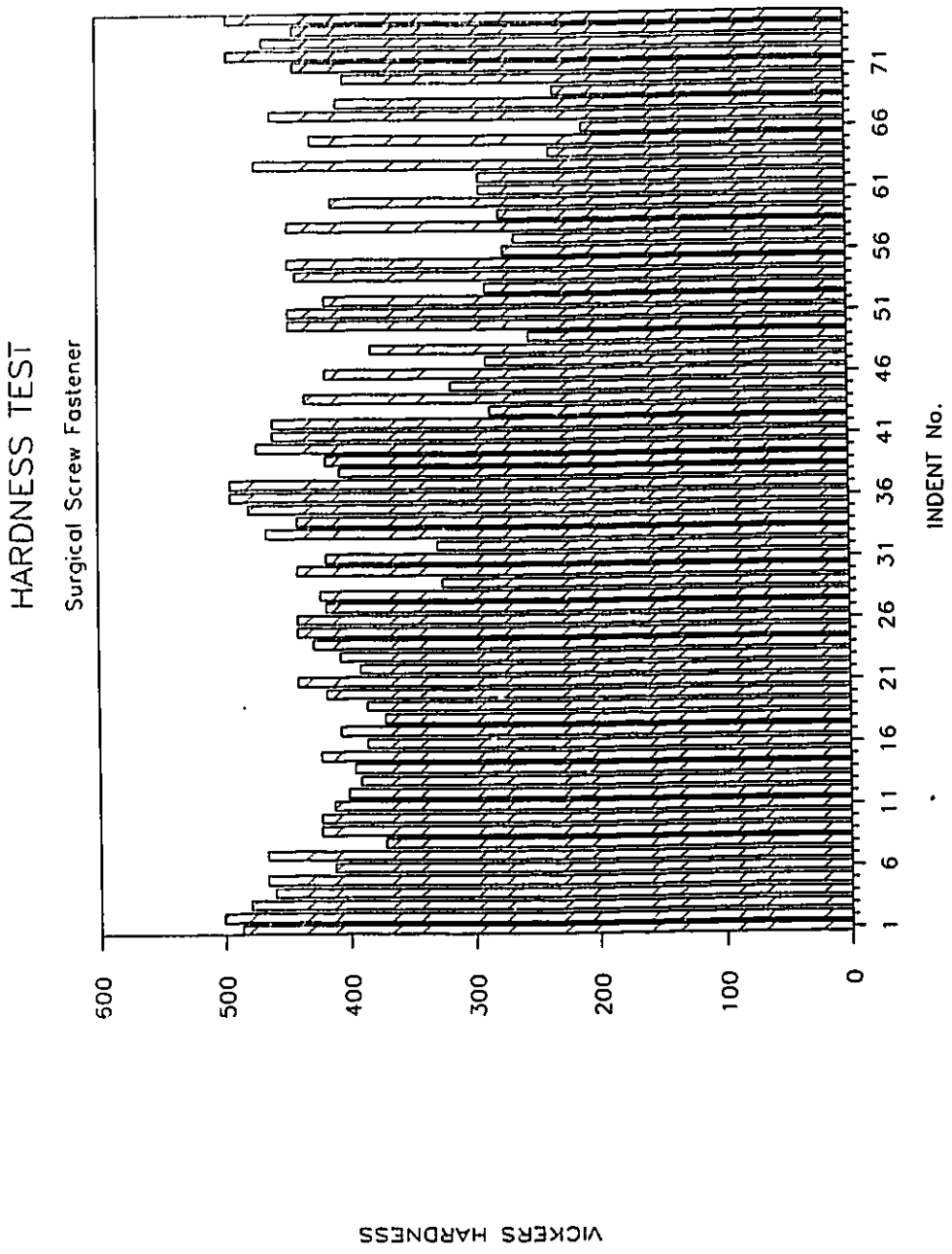

Figure 27 Vickers hardness versus position of traverse across section.

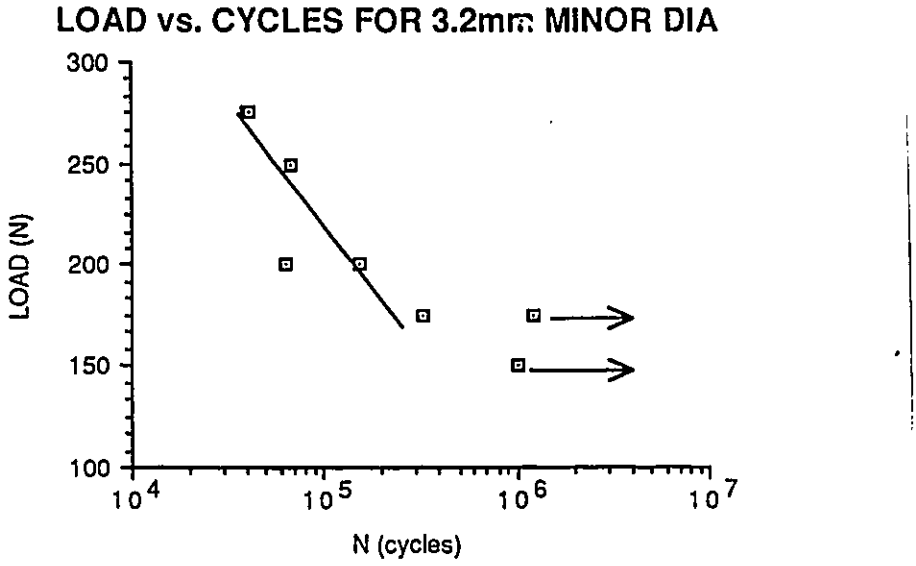

Figure 28. P-N curve for 3.2mm minor diameter screws.

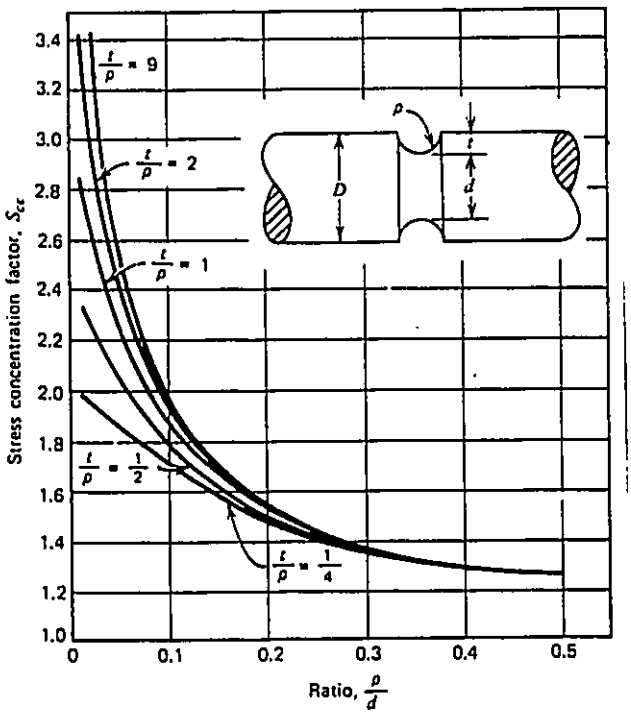

Figure 29. Neuber's curve for a circular shaft with semicircular grooves subjected to bending[6].

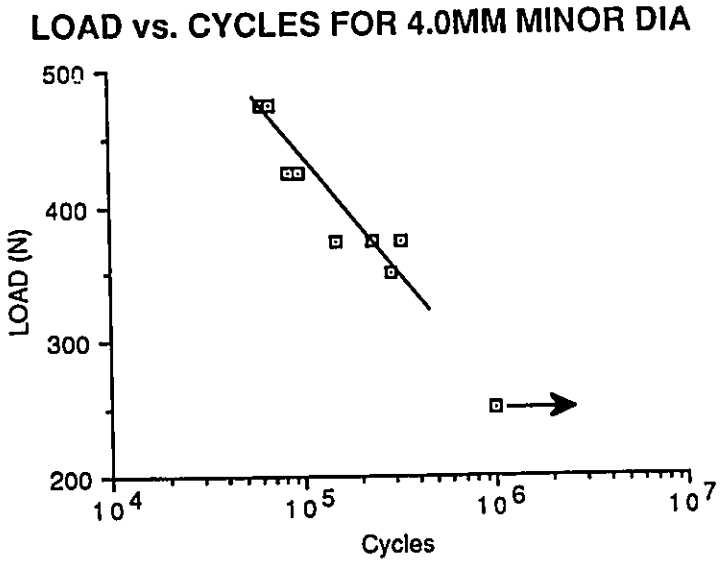

Figure 30 P-N curve for 4.0mm minor diameter screws.

APPENDIX 1.0

LIGHT MICROGRAPHS OF FAILED IMPLANTS

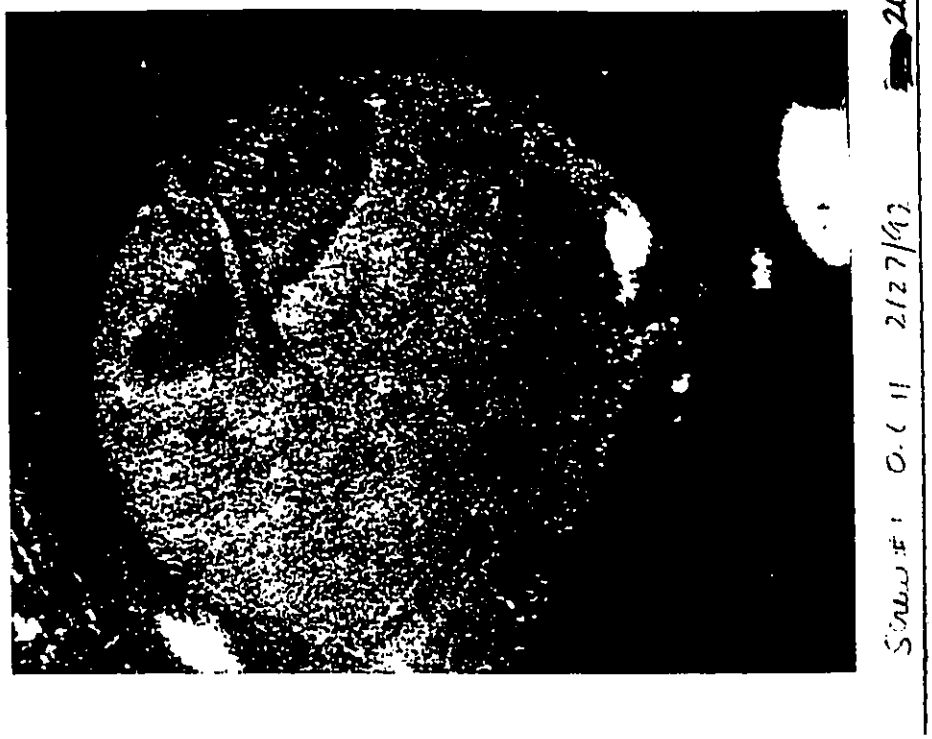

Failed Implant Screw #1 ; 26 times magnification

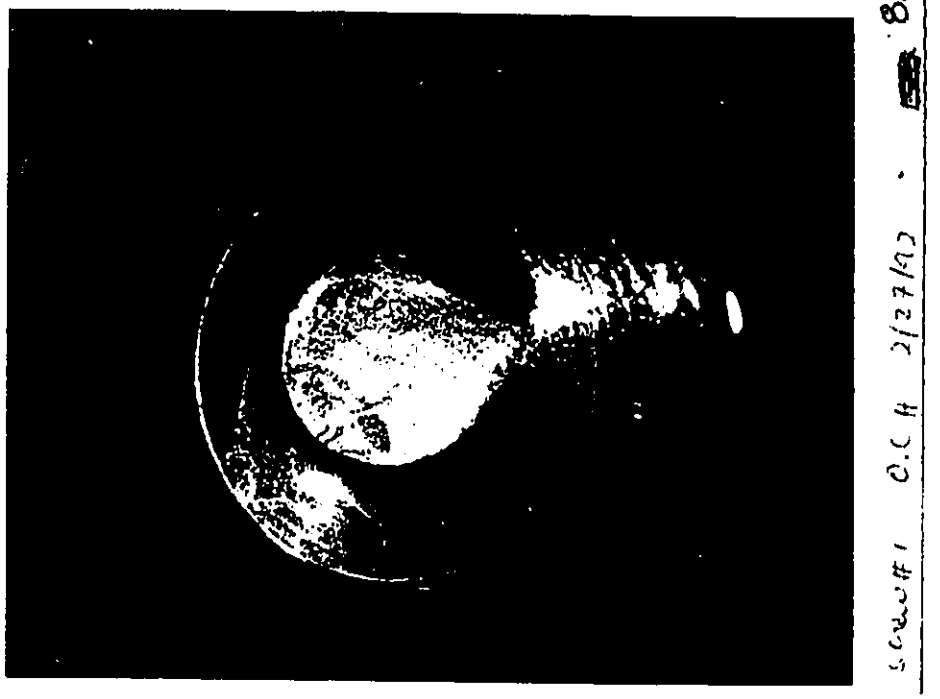

Failed Implant Screw #1 ; 8 times magnification

Failed Implant Screw #1 ; 20 times magnification

Failed Implant Screw #1 ; 26 times magnification

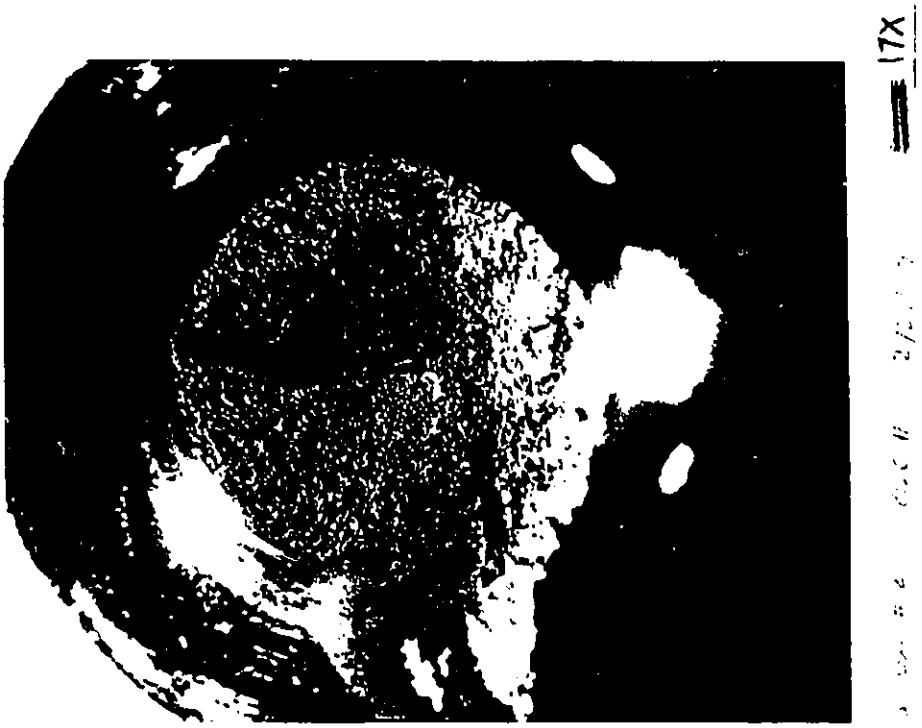

Failed Implant Screw #2 ; 17 times magnification

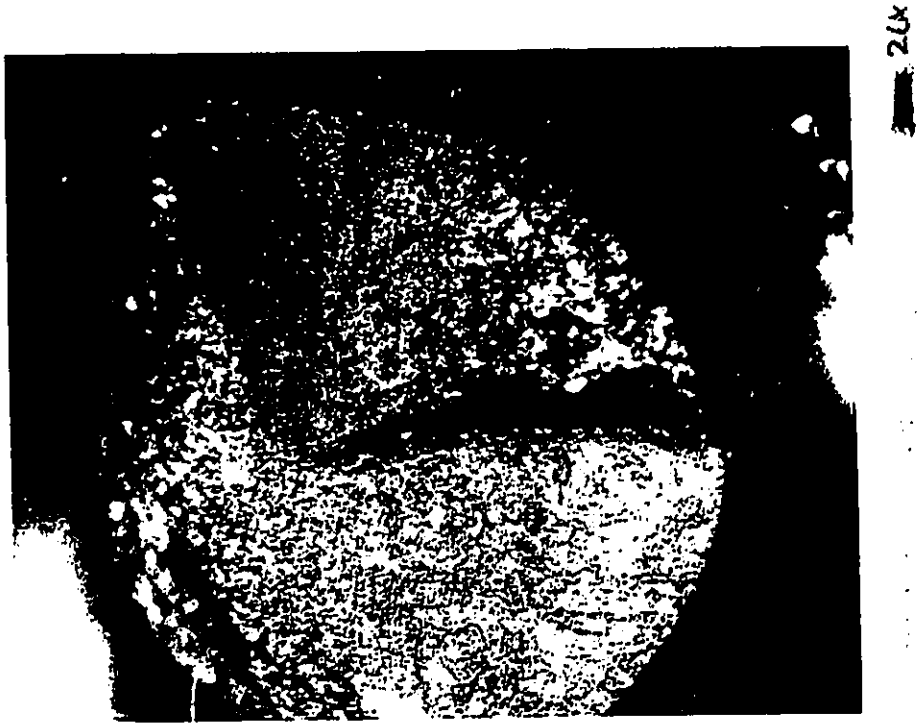

Failed Implant Screw #2 ; 26 times magnification

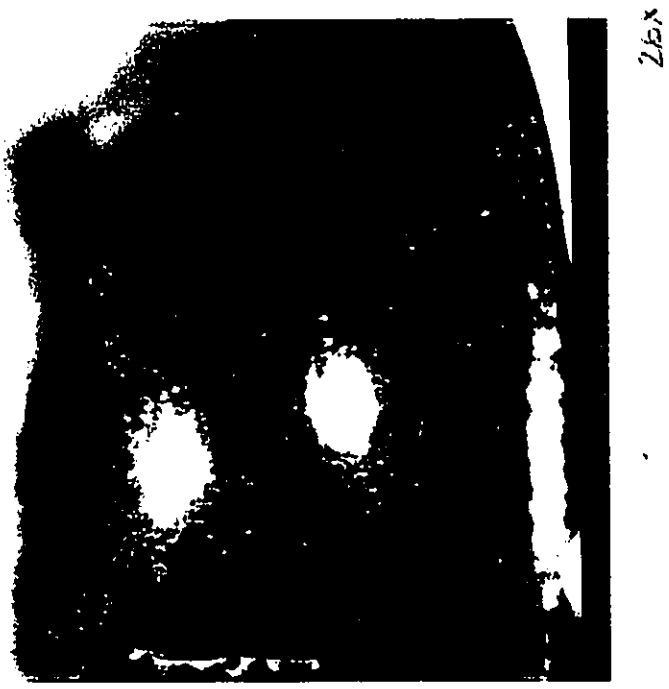

Failed Implant Screw #2 ; 26 times magnification

Failed Implant Screw #2 ; 13 times magnification

APPENDIX 2.0

SCANNING ELECTRON MICROGRAPHS OF FAILED IMPLANT

Failed Implant Screw #1 1.5mm from crack initation site

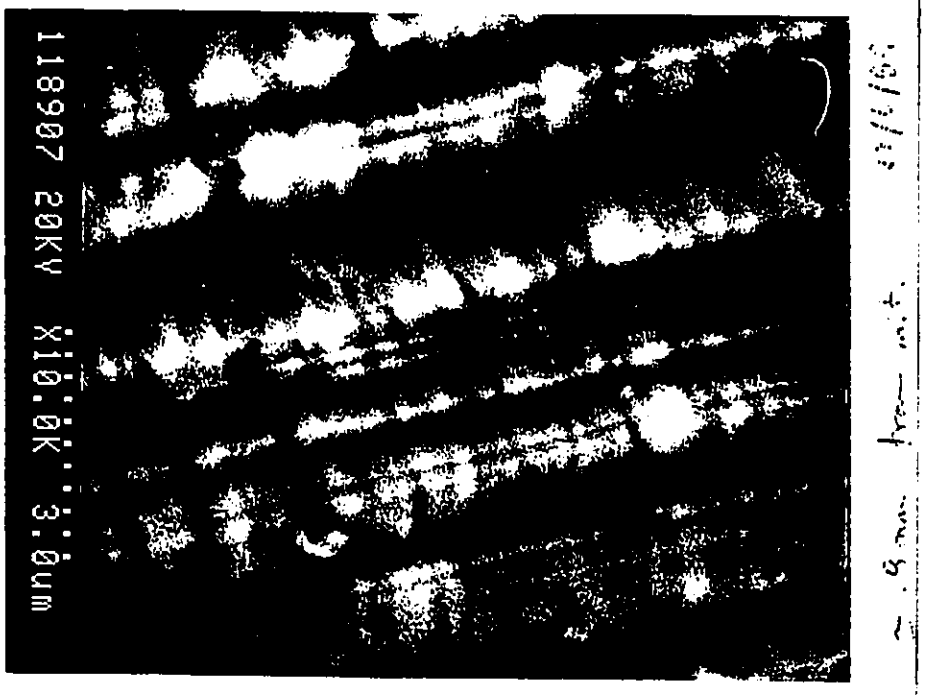

Failed Implant Screw #1 0.8mm from crack initation site

APPENDIX 3.0

VICKERS HARDNESS MEASUREMENTS

National Research Council Canada | Conseil national de recherches Canada

Page 1

NATIONAL AERONAUTICAL ESTABLISHMENT

STRUCTURES AND MATERIALS LABORATORY

Experiment No. _____

50 grams

Date _____

Name _____

Incr. # No.	$X_2 - X_1$	$Y_2 - Y_1$	Avg V.H		$X_2 - X_1$	$Y_2 - Y_1$	Avg V.H		$X_2 - X_1$	$Y_2 - Y_1$	Avg V.H	
1	14.2	[illegible]	13.9 / 467	21	14.9	14.1		41	14.5	13.8		
2	[illegible]	13.4	13.6 / 501	22	15.4	15.3		42	15.6	13.4		
3	14.3	13.4		23	15.1	15.0		[illegible]	[illegible]	17.5		
4	14.2	14.1		24	15.1	[illegible]		44	15.0	14.1		
5	14.0	14.1		25	14.6	14.3		45	17.4	16.8		
6	[illegible]	15.3		26	14.6	14.3		46	15.3	14.5		
7	[illegible]	14.5		27	15.4	[illegible]		47	[illegible]	17.8		
8	15.7	15.8		28	15.0	14.6		48	[illegible]	15.3		
9	14.1	15.1		29	16.0	17.8		49	[illegible]	[illegible]		
10	14.8	14.8		30	14.4	14.0		50	[illegible]	14.2		
11	15.0	15.0		31	14.9	15.0		51	[illegible]	14.8		
12	15.4	15.0		32	17.4	[illegible]		52	[illegible]	14.8		
13	15.4	15.3		33	14.9	[illegible]		53	[illegible]	[illegible]		
14	15.1	15.4		34	14.3	14.0		54	[illegible]	[illegible]		
15	15.0	14.5		35	14.7	[illegible]		55	[illegible]	14.3		
16	15.4	15.6		36	14.5	[illegible]		56	[illegible]	[illegible]		
17	[illegible]	15.2		37	14.4	13.0		57	[illegible]	13.2		
18	16.3	15.3		38	5.6	14.6		58	[illegible]	[illegible]		
19	14.9	16.1		39	15.3	[illegible]		59	[illegible]	18.1		
20	15.5	[illegible]		40	[illegible]	[illegible]		60	[illegible]	[illegible]		

National Research Council Canada | Conseil national de recherches Canada

NATIONAL AERONAUTICAL ESTABLISHMENT

STRUCTURES AND MATERIALS LABORATORY

Experiment No. _____

Date Dec 11/89

Name Bensk

Microhardness Testing (Dan R)

Indent No	$X_2 - X_1$	$Y_2 - Y_1$	Avg VH.									
61	17.5	18.0										
62	17.6	18.0										
63	14.8	13.1										
64	20.6	19.0										
65	15.1	14.2										
66	21.4	20.6										
67	14.4	13.9										
68	15.3	14.8										
69	13.7	13.4										
70	15.3	15.0										
71	14.3	14.6										
72	13.9	13.4										
73	14.4	13.7										
74	14.5	14.0										
75	13.9	13.5										
76												
77												
78												
79												

APPENDIX 4.0

CERTIFICATE OF TEST FOR 316LVM

AL Tech Specialty Steel Corporation

Willowbrook Avenue, Dunkirk, N.Y. 14048

CERTIFICATE OF TEST

PURCHASE ORDER NO AND DATE	ACCEPTING MILL	MILL ORDER NO	DATE SHIPPED	INVOICE
53353 06/27/08	DUNKIRK	6-2-20991		

SOLD TO: TERRAY MANUFACTURING INC
24 MCGONIGAL ST.WEST
ARNPRIOR,ONTARIO CANAD 11111
TR 3

SHIP TO: TERRAY MANUFACTURING INC
24 MCGONIGAL ST.WEST
ARNPRIOR,ONTARIO CANAD 11111
TR

PRODUCT SPECIFICATIONS: AL TECH STAINLESS STEEL TYPE CONS (AL-316-L)
ACD ASTM-F138-82 GR 2

ITEM	DESCRIPTION	QUANTITY	POUNDS	C/P
02	R .3125 12'		260	

CHEMICAL ANALYSIS — STANDARD ELEMENTS & PERCENTAGES

HEAT NO	C	MN	P	S	SI	CR	NI	AL	MO	CU	N2	V	W
23694	.016	1.44	.020	.001	.490	17.26	13.57		2.110	.180	.035		

ADDITIONAL ELEMENTS: CO .070

PHYSICAL PROPERTIES

HEAT NO	TENSILE KSI	YIELD KSI	% ELONG IN 2" OR 4D EQUIV.	RED AREA %	HARDNESS RC	GS	FERRITE	MAGNAFLUX TEST NO	CH IMP
23694 INGOT 15	183.0 1256mPa	148.0 1016MPa	17.0	64.0	35.0	5-6			

CAPABILITIES

HARDENABILITY

MATERIAL FREE FROM FERRITE AT 100X

MATERIAL CAPABLE OF PRACTICE E ASTM-A262

MACRO ETCH TEST-O.K.
MICRO TEST-O.K.

JK RATING	A	B	C	D
THIN	1.0	0.0	0.0	1.(
HEAVY	0.0	0.0	0.0	0.(

TEST CERTIFIER

APPENDIX 5.0

SAMPLE CALCULATIONS

5.1 Analysis of Striation Spacing

The crack propagation rate da/dN was determined by counting the number of cycles over a given length at .8mm from the crack tip.

14 cycles=6.35cm

The magnification factor is indicated at the bottom of the micrograph.

3.1cm = 3 micrometers

Crack Growth Rate for 14 cycles

$$\frac{da}{dN}=\left(\frac{6.35cm}{14cycles}\right)\left(\frac{3\mu m}{3.1cm}\right)\left(\frac{1m}{1x10^{6}\mu m}\right)=4.389x10^{-7}\frac{m}{cycle}$$

$$\frac{da}{dN}=4.389x10^{-7}\frac{m}{cycle}\left(\frac{100cm}{1m}\right)\left(\frac{1inch}{2.54cm}\right)=1.728x10^{-5}\frac{inch}{cycle}$$

Stress Intensity Range is given from equation 26

$$\frac{da}{dN}=3.0x10^{-10}(\Delta K_1)^{3.25}$$

$$\Delta K=\left(\frac{da/dN}{3.0x10^{-10}}\right)^{\frac{1}{3.25}}$$

$$\Delta K=\left(\frac{1.728x10^{-6}}{3.0x10^{-10}}\right)^{\frac{1}{3.25}}=29.16Ksi\sqrt{inch}$$

$$29.16Ksi\sqrt{inch}\left(\frac{6.895MPa}{1Ksi}\right)\left(\frac{2.54}{1inch}\right)^{1/2}\left(\frac{1m}{100cm}\right)^{1/2}=32.04MPa\sqrt{m}$$

As noted in section 2.4 this relation is for 316 in the 20% cold worked condition. A value of 20 $MPam^{1/2}$ is assumed for the 60% cold worked condition.

Assuming the solution for a circular arc edge crack in a bar under bending

$$\Delta K = .75\Delta\sigma\sqrt{\pi a}$$

$$\Delta\sigma = \frac{\Delta K}{.75\sqrt{\pi a}}$$

For 20% CW

$$\Delta\sigma = \frac{32.04MPa\sqrt{m}}{.75\sqrt{\pi .0008m}} = 852MPa$$

For 60% CW

$$\Delta\sigma = \frac{20.00MPa\sqrt{m}}{.75\sqrt{\pi .0008m}} = 531MPa$$

Assuming R=.1

$$\Delta\sigma = \sigma_{max} - \sigma_{min} = \sigma_{max}(1-.1)$$

For 20% CW

$$\sigma_{max} = \frac{\Delta\sigma}{(1-.1)} = \frac{852Mpa}{.9} = 946Mpa$$

For 60% CW

$$\sigma_{max} = \frac{\Delta\sigma}{(1-.1)} = \frac{531Mpa}{.9} = 590Mpa$$

Assuming K=1.5

For 20% CW

$$\sigma_{nom}=\frac{\sigma_{max}}{K}=\frac{946MPa}{1.5}=630MPa$$

For 60% CW

$$\sigma_{nom}=\frac{\sigma_{max}}{K}=\frac{590MPa}{1.5}=393MPa$$

For a circular shaft in bending the bending stress is given by the flexure formula from equation 8 which yields

$$\sigma=\frac{32M}{\pi d_e^3}$$

where d_e is the effective diameter. The tensile stress area from equation 29 is given by

$$A_t=\frac{\pi}{4}\left(d-\frac{.9743}{n}\right)^2=\frac{\pi}{4}\left(.256-\frac{.9743}{9.26}\right)^2=.017inch^2$$

where n=1/.108".

The effective diameter d_e can then be obtained from

$$A=\pi r^2=\frac{\pi d^2}{4}\ ;\ d=\left(\frac{4A}{\pi}\right)^{1/2}$$

$$d_e=\left(\frac{4A_t}{\pi}\right)^{1/2}=\left(\frac{4x.017}{\pi}\right)^{1/2}=.147inch=3.74mm$$

20% CW

$$M=\frac{\sigma\pi d_e^3}{32}=\frac{(630\times10^6)\ (\pi)\ (3.74\times10^{-3}m)^3}{32}=3.23Nm$$

For 60% CW

$$M=\frac{\sigma\pi d_e^3}{32}=(\frac{393\times10^6)\ (\pi)\ (3.74\times10^{-3}m)^3}{32}=2.02Nm$$

Using the definition of bending moment for 3 point bending at midlength

$$M=(\frac{P}{2})\ (\frac{l}{2})$$

and for this case d=17.15mm, we calculate the magnitude of the equivalent force P. Rearranging and solving for P, we obtain

For 20% CW

$$P=\frac{(2)\ (3.23Nm)}{.01715}=376N$$

For 60% CW

$$P=\frac{(2)\ (2.02Nm)}{.01715}=235N$$

Assuming the solution for a semielliptical surface crack in a shaft under bending from equation 16

$$\Delta K_{B,I,3}=\Delta\sigma\sqrt{\pi b}F_{B,I,3}$$

where

$$F_{B,I,3}=F_{T,I,3}\frac{F_{B,I,2}}{F_{T,I,2}}$$

First we need to calculate the values for $F_{T,I,3}$from equation 18

$$F_{T,I,3}=B\times\Lambda$$

where

$$B=1.122-0.23\beta-0.901\beta^2+0.949\beta^3-0.28\beta^4$$

From the micrograph where the crack length =.8mm, the crack width was measured and found to be 2a=2.3mm and thus a=1.15mm. Substituting this value into the equation we obtain

$$\beta=\frac{b}{a}=\frac{.8mm}{1.15mm}=.697$$

$$B=1.122-0.230(.697)-0.901(.697)^2+0.949(.697)^3-0.280(.697)^4=$$

and

$$\Lambda=1.0+0.157\lambda-0.634\lambda^2+4.59\lambda^3-6.628\lambda^4$$

$$\lambda=\frac{a}{D}=\frac{1.15mm}{3.74mm}=.307$$

$$\Lambda=1.0+0.157(.307)-0.634(.307)^2+4.59(.307)^3-6.628(.307)^4=1.0$$

$$F_{T,I,3}=B\times\Lambda=.780x1.06=.827$$

Next, we need to determine the values for $F_{B,I,2}$ and $F_{T,I,2}$. Recalling that b/d=.8/3.2=.25 and c/W=.25 so that

$$\lambda = \frac{c}{W} = .25$$

Substituting this values into equation 21,

$$F_{B,I,2} = 1.121 - 1.199\lambda + 4.775\lambda^2 - 1.628\lambda^3 - 7.035\lambda^4 + 13.27\lambda^5$$

we obtain

$$F_{B,I,2} = 1.121 - 1.199(.25) + 4.775(.25)^2 - 1.628(.25)^3 -$$

$$7.035(.25)^4 + 13.27(.25)^5 = 1.08$$

and equation 22

$$F_{T,I,2} = 1.12 - 0.231\lambda + 10.55\lambda^2 - 21.72\lambda^3 + 30.39\lambda^4$$

$$F_{T,I,2} = 1.12 - 0.231(.25) + 10.55(.25)^2 - 21.72(.25)^3 + 30.39(.25)^4$$

$$F_{T,I,2} = 1.50$$

Substituting these values into equation 17 we obtain

$$F_{B,I,3} = F_{T,I,3}\frac{F_{B,I,2}}{F_{T,I,2}} = (.827)\frac{(1.08)}{(1.50)} = .595$$

Substituting this value into equation 16 we obtain

$$\Delta\sigma = \frac{\Delta K}{.595\sqrt{\pi a}}$$

For 20% CW

$$\Delta\sigma = \frac{32.04MPa\sqrt{m}}{.595\sqrt{\pi .0008m}} = 1074MPa$$

For 60% CW

$$\Delta\sigma = \frac{20.00MPa\sqrt{m}}{.595\sqrt{\pi .0008m}} = 670MPa$$

Assuming R=.1

$$\Delta\sigma = \sigma_{max} - \sigma_{min} = \sigma_{max}(1-.1)$$

For 20% CW

$$\sigma_{max} = \frac{\Delta\sigma}{(1-.1)} = \frac{1074Mpa}{.9} = 1193Mpa$$

For 60% CW

$$\sigma_{max} = \frac{\Delta\sigma}{(1-.1)} = \frac{670Mpa}{.9} = 744Mpa$$

Assuming K=1.5

For 20% CW

$$\sigma_{nom} = \frac{\sigma_{max}}{K} = \frac{1193MPa}{1.5} = 795MPa$$

For 60% CW

$$\sigma_{nom} = \frac{\sigma_{max}}{K} = \frac{744MPa}{1.5} = 496MPa$$

For 20% CW

$$M=\frac{\sigma\pi d_e^3}{32}=(\frac{795\times10^6)\ (\pi)\ (3.74\times10^{-3}m)^3}{32}=4.08Nm$$

For 60% CW

$$M=\frac{\sigma\pi d_e^3}{32}=(\frac{496\times10^6)\ (\pi)\ (3.74\times10^{-3}m)^3}{32}=2.54Nm$$

Using the definition of bending moment for 3 point bending at midlength

$$M=(\frac{P}{2})\ (\frac{l}{2})$$

and for this case d=17.15mm, we calculate the magnitude of the equivalent force P. Rearranging and solving for P, we obtain

For 20% CW

$$P=\frac{(2)\ (4.08Nm)}{.01715}=476N$$

For 60% CW

$$P=\frac{(2)\ (2.54Nm)}{.01715}=297N$$

5.2 Validity of LEFM

The applicability of Linear Elastic Fracture Mechanics is determined by comparing the plastic zone size r_p to the material thickness t where from equation 25 we obtain

$$r_p=\frac{1}{24\pi}(\Delta K/\sigma_{ys})^2 \; ; \; \sigma_{ys}=1016MPa \; ; \; \Delta K32.04MPa\sqrt{m}$$

$$r_p=\frac{1}{24\pi}(\frac{32.04MPa\sqrt{m}}{1016MPa})^2=1.319x10^{-5}m$$

For plane strain conditions

$$\frac{r_p}{t}<50 \; ; \; t=3.2mm=.0032m$$

$$\frac{r_p}{t}=\frac{1.319x10^{-5}}{.0032}=.004$$

5.3 3.2mm Root Diameter Test Coupons

The nominal bending stress in column 2 of table 5 was calculated using equation 8 where for three point bending at midlength, the bending moment is given by

$$M=(\frac{P}{2})(\frac{l}{2})$$

For specimen number one in table 4, l=.0635m and P=250N. Recalling, that the effective diameter was calculated in 5.1 of this appendix and substituting these values into equation 8 we obtain the nominal bending stress

$$\sigma=\frac{32(P/2)(l/2)}{\pi d^3}=\frac{32(250N/2)(.0635m/2)}{\pi(3.74x10^{-3}m)^3}=773MPa$$

In order to establish the relationship between the cycles to failure and the maximum stress, we must first solve for the constants A and B in equation 9

$$A=\sigma_R L^B$$

Taking the log of this equation, we obtain

$$\log A=\log\sigma_R+B\log L$$

We require two sets of points to solve for constants A and B. The first point occurs at the following

$$at L=1000\ ;\ \sigma_R=.9\sigma_{ult}=.9(1261)=1135 MPa$$

$$\log A=\log 1135+B\log 1000=3.055+3B$$

We require the endurance limit of the material for the second point which is obtained from the material's Ultimate Strength from the following

$$\sigma_{ult}=1261 MPa\ ;\ \sigma_e=.58\sigma_{ult}=.58(1261)=731 Mpa$$

Substituting into Basquin's Equation, the second point occurs at the following

$$at L=1,000,000\ ;\ \sigma_e=731 Mpa$$

$$log A=log 731 Mpa+B\log 1,000,000=2.864+6B$$

Solving for A and B from the two equations we obtain
log A=3.246 and B=.0637

$$3.246=\log\sigma_R+.0637 log L$$

Now that we have established the values for A and B, we can solve for the equivalent completely reversing stress. For specimen #1, L=68,620 cycles

$$\log\sigma_R = 3.246 - .0637\log 68{,}720 = 2.938$$

$$\sigma_R = 867 MPa$$

We can now solve for the maximum stress from equation 7

$$0.45\sigma_{max}^2\sigma_{ult} + .55\sigma_{max}\sigma_{nom}\sigma_R - \sigma_{nom}\sigma_R\sigma_{ult} = 0$$

Substituting in the appropriate values we obtain

$$0.45\sigma_{max}^2(1261) + .55\sigma_{max}(773)(867) - (867)(773)(1261) = 0$$

We now must solve for the roots of this equation from

$$\frac{-b \pm \sqrt{b^2 - 4ac}}{2a}$$

$$\frac{-(.55)(773)(867) \pm \sqrt{(.55*773*867)^2 + 4(.45)(1261)(867)(773)(12}}{2(.45)(1261)}$$

$$\sigma_{max} = 938 MPa \; ; \; \sigma_{max} = -1587 MPa$$

Solving for the experimental stress concentration factor we obtain

$$K = \frac{\sigma_{max}}{\sigma_{nom}} = \frac{938}{764} = 1.21$$

The theoretical stress concentration factor is obtained by calculating the following geometric factors for a shaft with semicircular grooves subjected to bending

$$\rho = .76 mm \; ; \; t = 3.3 mm \; ; \; d = 3.2 mm$$

$$\frac{\rho}{d}=\frac{.76}{3.2}=.24 \;;\; \frac{t}{\rho}=\frac{3.3}{.76}=4.3$$

From figure 12-2.9 [6], K_t=1.5

The notch sensitivity index is given by equation 1

$$q=\frac{K_f-1}{K_t-1}$$

rearranging

$$K_f=q(K_t-1)+1$$

For a shaft in bending with a semicircular groove, q=.8[6]

$$K_f=q(K_t-1)+1=.8(1.5-1)+1=1.40$$

The maximum shear stress can be obtained from the maximum shear theory of failure from any strength of materials text where the maximum shear is related to the maximum normal stress according to

$$\tau_{max}=\frac{1}{2}\sigma$$

Substituting in the value of the maximum stress, we obtain

$$\tau_{max}=\frac{1}{2}(938MPa)=469MPa$$

5.4 Test Coupon Elongation Due to Bending

The test coupon elongation due to bending was calculated to determine the change in length l of the 3 point bend specimens. For simply supported beams subjected to a point load [25]

$$y_{max}=\frac{Pl^3}{48EI}\left(1+\frac{31.2\alpha I}{l^2A}\right)$$

For the 3.2mm minor diameter screw

$$P=275N\ ;\ d=3.74mm\ ;\ A=\frac{\pi d^2}{4}\ ;\ I=\frac{\pi d^4}{64}$$

$$\alpha=\frac{4}{3}\ for\ circular\ cross\ sections\ ;\ E=193,100Mpa\ ;\ l=.0635m$$

Substituting these values into the deflection equation we obtain

$$y_{max}=\frac{(250N)\,(.0635m)^3}{48\,(193.1x10^9Pa)\,\pi\frac{(.00374m)^4}{64}}\left(1+\frac{31.2\,(4/3)\,\pi\frac{(.00374m)^4}{64}}{(.0635)^2\pi\frac{(.00374m)^2}{4}}\right)$$

$$y_{max}=7.39x10^{-4}m$$

Approximating the deflected length as a triangle and solving for the hypotenuse

$$hyp=\sqrt{x^2+Y^2}$$

where

$$x=\frac{l}{2}=\frac{.0635m}{2}=.03175m\ ;\ y=7.39x10^{-4}m$$

$$hyp=\sqrt{(.03175m)^2+(7.39x10^{-4})^2}=.0317586m$$

The TCE is then the difference between the deflected and undeflected length as follows

$$TCE=2(.0317586)-.0635=1.72x10^{-5}m$$

For the 4.0mm minor diameter screw

$$P=475N\ ;\ d=4.0mm$$

Substituting these values into the deflection equation we obtain

$$y_{max}=\frac{(475N)(.0635m)^3}{48(193.1x10^9Pa)\pi\frac{(.004m)^4}{64}}\left(1+\frac{31.2(4/3)\pi\frac{(.004m)^4}{64}}{(.0635)^2\pi\frac{(.004m)^2}{4}}\right)$$

$$y_{max}=1.05x10^{-3}m$$

Approximating the deflected length as a triangle and solving for the hypotenuse

$$hyp=\sqrt{x^2+Y^2}$$

where

$$x=\frac{l}{2}=\frac{.0635m}{2}=.03175m\ ;\ y=1.05x10^{-3}m$$

$$hyp=\sqrt{(.03175m)^2+(1.05x10^{-3})^2}=.0317675m$$

The TCE is then the difference between the deflected and undeflected length as follows

$$TCE=2(.0317675)-.0635=3.50x10^{-5}m$$

5.5 Estimate of Cycles to Failure for 4.0mm Specimens

The tensile stress area is given by equation 29 where n=1/.118".

$$A_t=\frac{\pi}{4}\left(d-\frac{.9743}{n}\right)^2=\frac{\pi}{4}\left(.256-\frac{.9743}{8.47}\right)^2=.016\,inch^2$$

The effective diameter d_e can then be obtained from

$$A=\pi r^2=\frac{\pi d^2}{4}\ ;\ d=\left(\frac{4A}{\pi}\right)^{1/2}$$

$$d_e=\left(\frac{4A_t}{\pi}\right)^{1/2}=\left(\frac{4x.016}{\pi}\right)^{1/2}=.147\,inch=3.58mm$$

Taking the ratio of the 3.2mm specimen we obtain

$$\frac{3.2mm}{3.74mm}=\frac{4.0mm}{x}\ ;\ x=4.68mm$$

The theoretical stress concentration factor is obtained by calculating the following geometric factors for a shaft with semicircular grooves subjected to bending

$$\rho=.76mm\ ;\ t=3.3mm\ ;\ d=4.0mm$$

$$\frac{\rho}{d}=\frac{.76}{4.0}=.19\ ;\ \frac{t}{\rho}=\frac{2.5}{.75}=3.33$$

From figure 12-2.9[6], K_t=1.6.

Taking the ratio of the theoretical to experimental stress concentrations for the 3.2mm specimens we obtain

$$\frac{1.4}{1.28}=\frac{1.6}{x} \; ; \; x=1.45$$

There is a reduction in the stress concentration factor due to the .010" increase in pitch[11]. Assuming a K_t=1.4

$$\sigma_{nom}=\frac{32\,(P/2)\,(l/2)}{\pi d^3}=\frac{32\,(375N/2)\,(.0635m/2)}{\pi\,(4.68x10^{-3}m)^3}=592MPa$$

$$\sigma_{max}=K\sigma_{nom}=1.40\,(592)=829MPa$$

$$\sigma_r=.45\sigma_{max}=.45\,(829MPa)=373MPa$$

$$\sigma_{avg}=.55\sigma_{max}=.55\,(829MPa)=456MPa$$

$$\sigma_R=\frac{K\sigma_r\sigma_{ult}}{\sigma_{ult}-\sigma_{avg}}=\frac{1.4\,(373)\,(1261)}{(1261-456)}=819MPa$$

$$logL=\frac{3.246-log\sigma_R}{.0637}=\frac{3.246-log819}{.0637}=5.223 \; ; \; L=167,175\ cycles$$

APPENDIX 6.0

LIGHT MICROGRAPHS OF 3.2mm TEST COUPONS

Test Coupon #1 3.2mm root diameter ; cycles to failure N=68,720

Test Coupon #1 3.2mm root diameter ; cycles to failure N=68,720

Test Coupon #2 3.2mm root diameter ; cycles to failure N=63,540

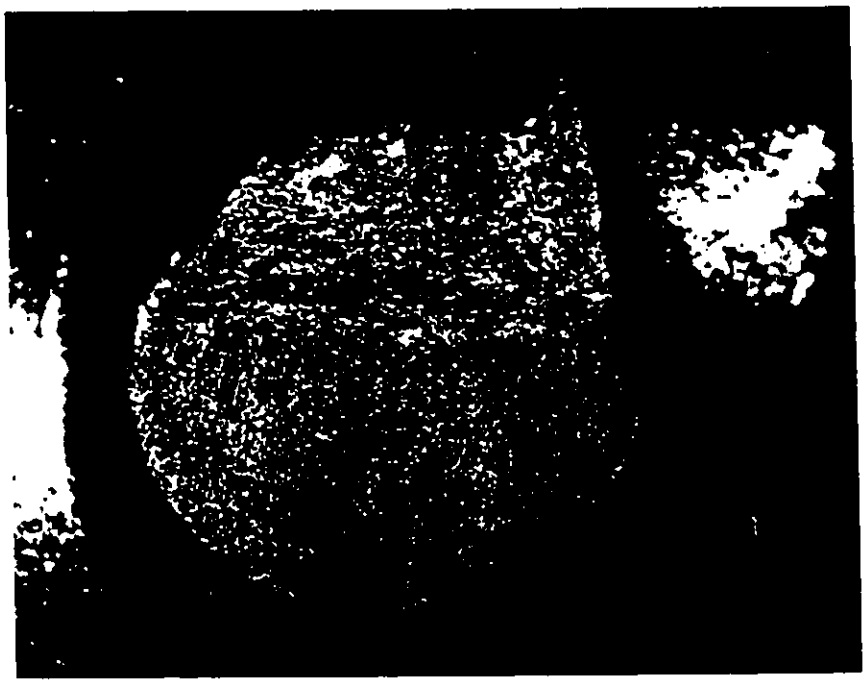

Test Coupon #2 3.2mm root diameter ; cycles to failure N=63,540

Test Coupon #3 3.2mm root diameter ; cycles to failure N=266,190

Test Coupon #3 3.2mm root diameter ; cycles to failure N=266,190

Test Coupon #4 3.2mm root diameter ; cycles to failure N=155,680

Test Coupon #4 3.2mm root diameter ; cycles to failure N=155,680

Test Coupon #5 3.2mm root diameter ; cycles to failure N=40,290

Test Coupon #2 3.2mm root diameter ; cycles to failure N=40,290

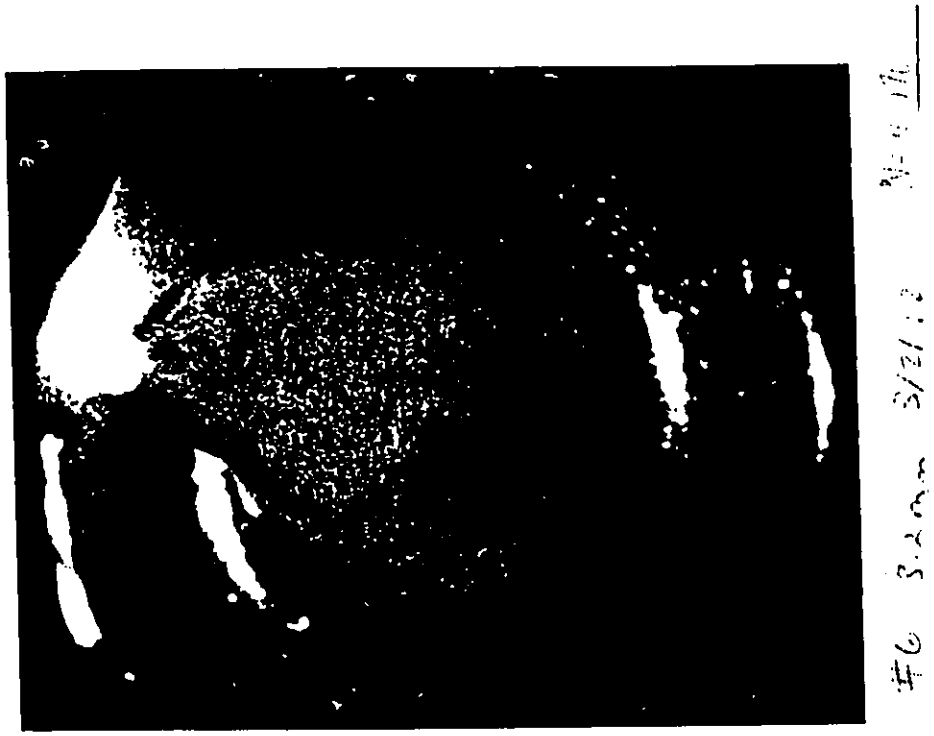

Test Coupon #6 3.2mm root diameter ; cycles to failure N=41,170

Test Coupon #6 3.2mm root diameter ; cycles to failure N=41,170

Test Coupon #8 3.2mm root diameter ; cycles to failure N=323,620

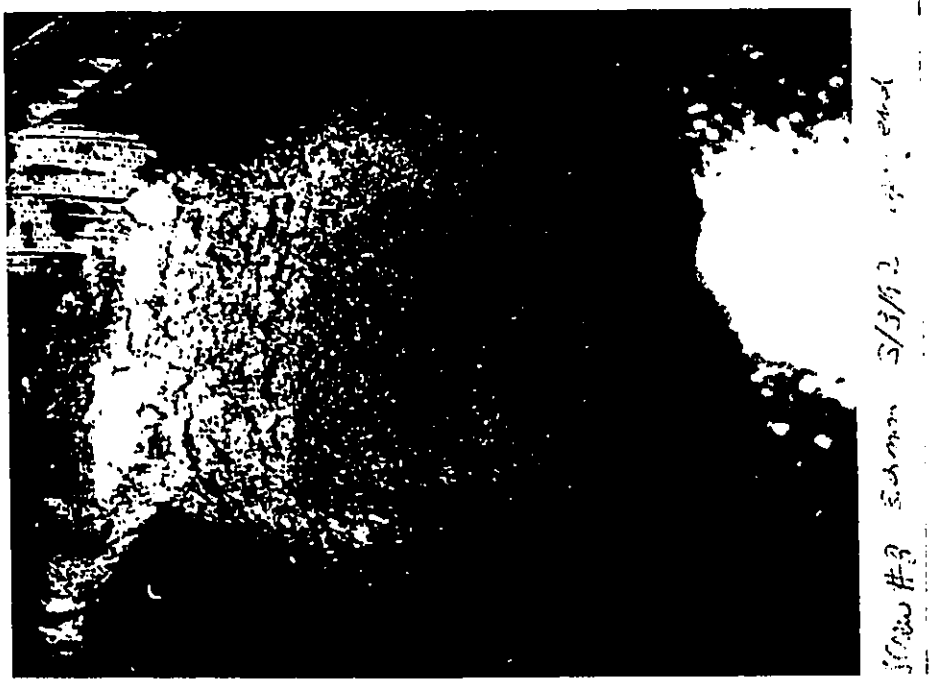

Test Coupon #8 3.2mm root diameter ; cycles to failure N=323,620

APPENDIX 7.0

SCANNING ELECTRON MICROGRAPHS OF 3.2mm TEST COUPONS

Test Coupon #2 3.2mm root diameter ; .091mm from crack initiation site.

Test Coupon #2 3.2mm root diameter ; .518mm from crack initiation site.

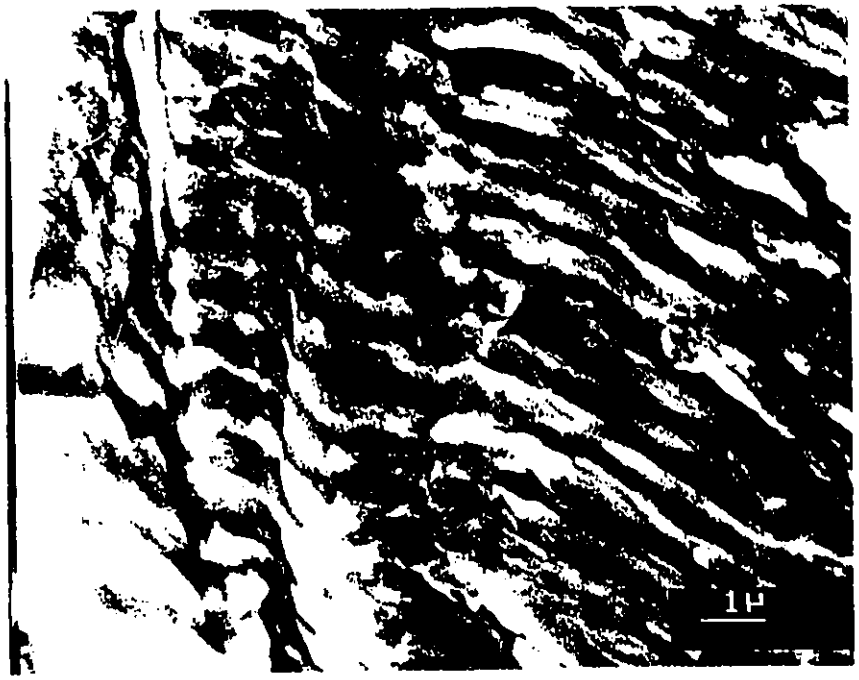

Test Coupon #2 3.2mm root diameter ; 1.09mm from crack initiation site.

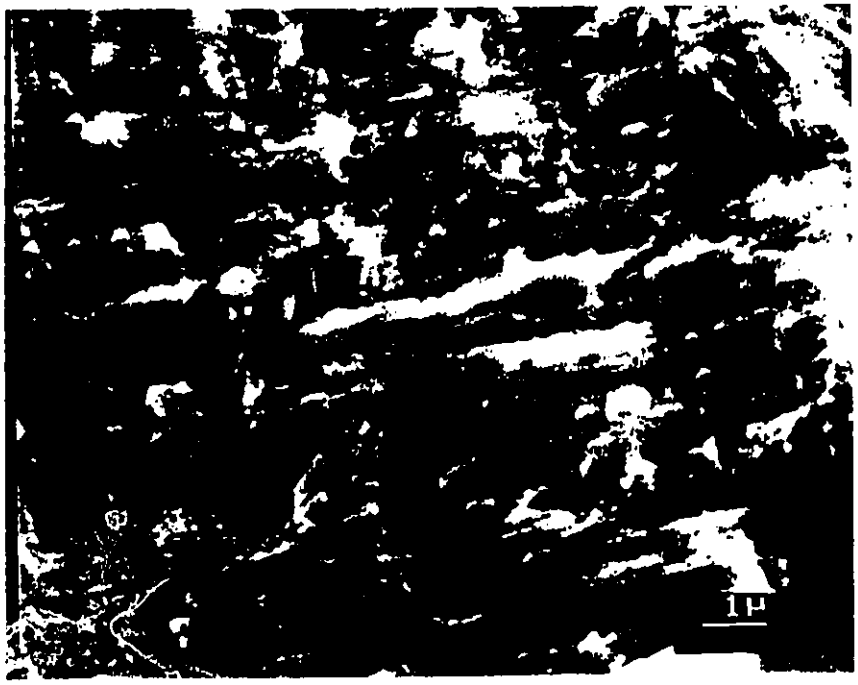

Test Coupon #4 3.2mm root diameter ; .416mm from crack initiation site.

Test Coupon #4 3.2mm root diameter ; .322mm from crack initiation site.

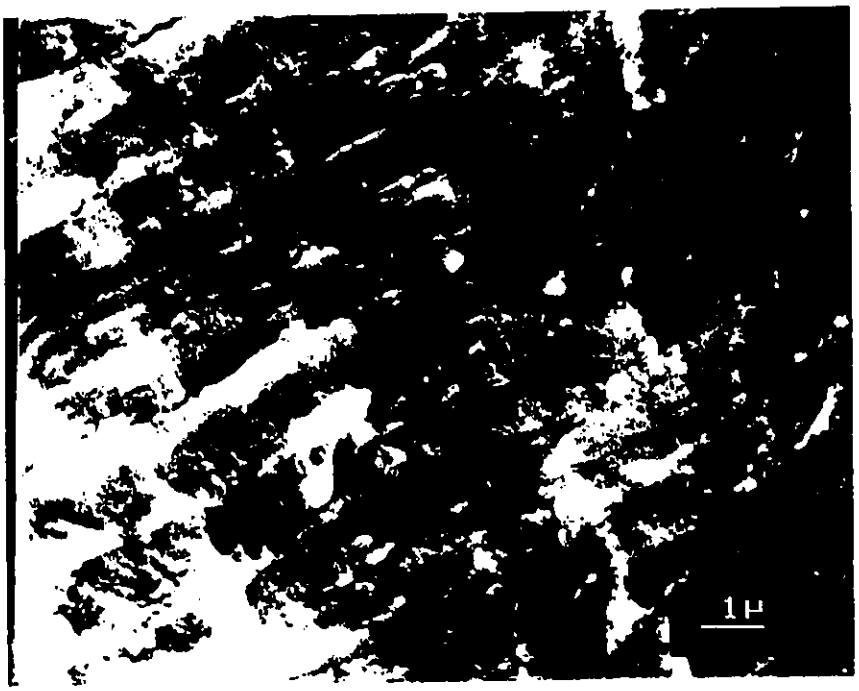

Test Coupon #4 3.2mm root diameter ; .332mm from crack initiation site.

Test Coupon #8 3.2mm root diameter ; .337mm from crack initiation site.

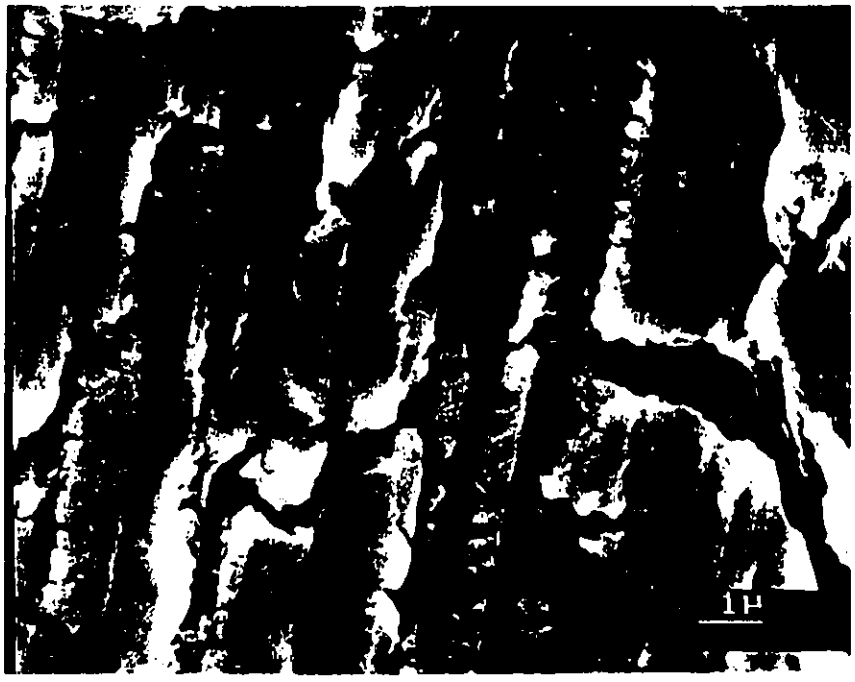

Test Coupon #8 3.2mm root diameter ; .789mm from crack initiation site.

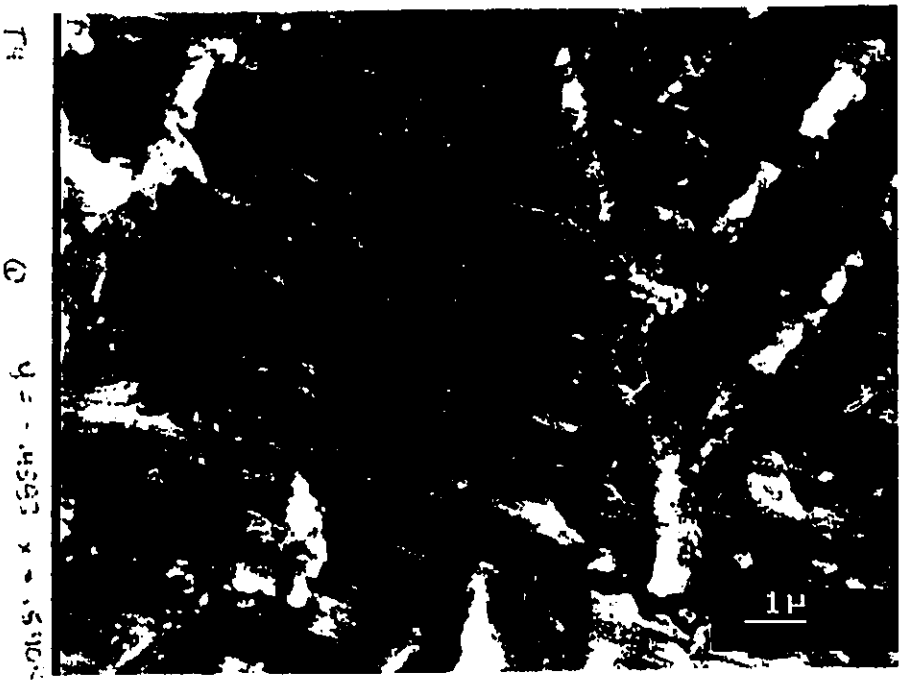

Test Coupon #3 3.2mm root diameter ; .185mm from crack initiation site.

APPENDIX 8.0

LIGHT MICROGRAPHS OF 4.0mm TEST COUPONS

Test Coupon #1 4.0mm root diameter ; cycles to failure N=232,440

Test Coupon #1 4.0mm root diameter ; cycles to failure N=232,440

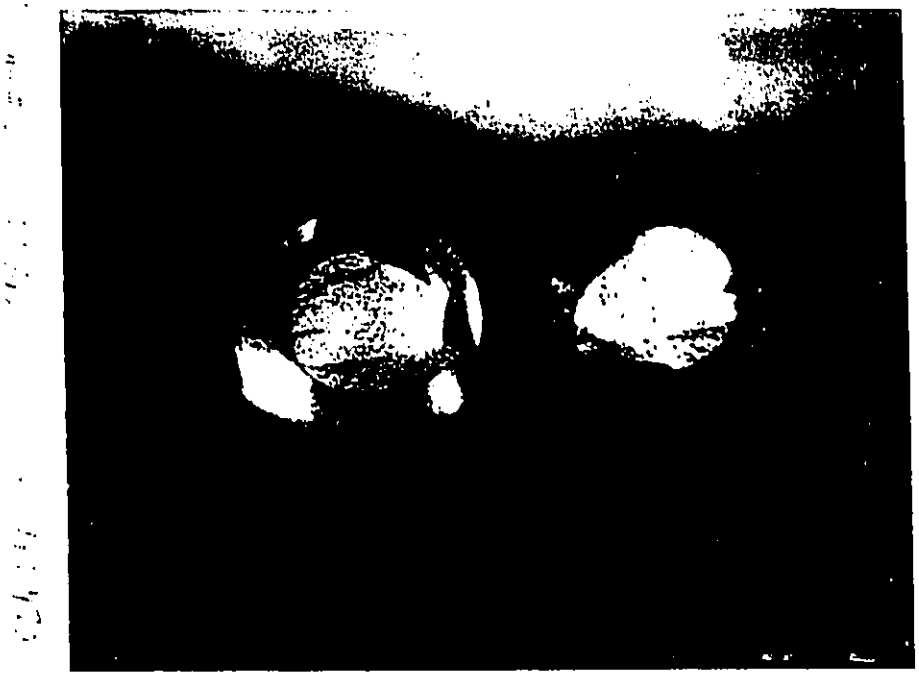

Test Coupon #2 4.0mm root diameter ; cycles to failure N=149,470

Test Coupon #2 4.0mm root diameter ; cycles to failure N=149,470

Test Coupon #3 4 0mm root diameter ; cycles to failure N=335,370

Test Coupon #3 4.0mm root diameter ; cycles to failure N=335,370

Test Coupon #4 4.0mm root diameter ; cycles to failure N=84,360

Test Coupon #4 4.0mm root diameter ; cycles to failure N=84,360

Test Coupon #5 4.0mm root diameter ; cycles to failure N=97,520

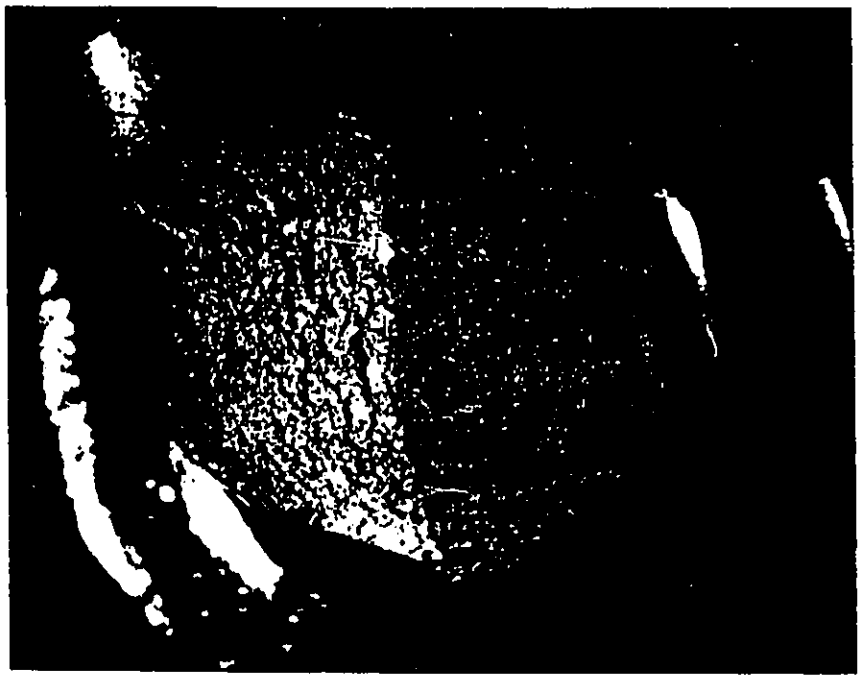

Test Coupon #5 4.0mm root diameter ; cycles to failure N=97,520

Test Coupon #6 4.0mm root diameter ; cycles to failure N=68,380

Test Coupon #6 4.0mm root diameter ; cycles to failure N=68,380

Test Coupon #7 4.0mm root diameter ; cycles to failure N=68,380

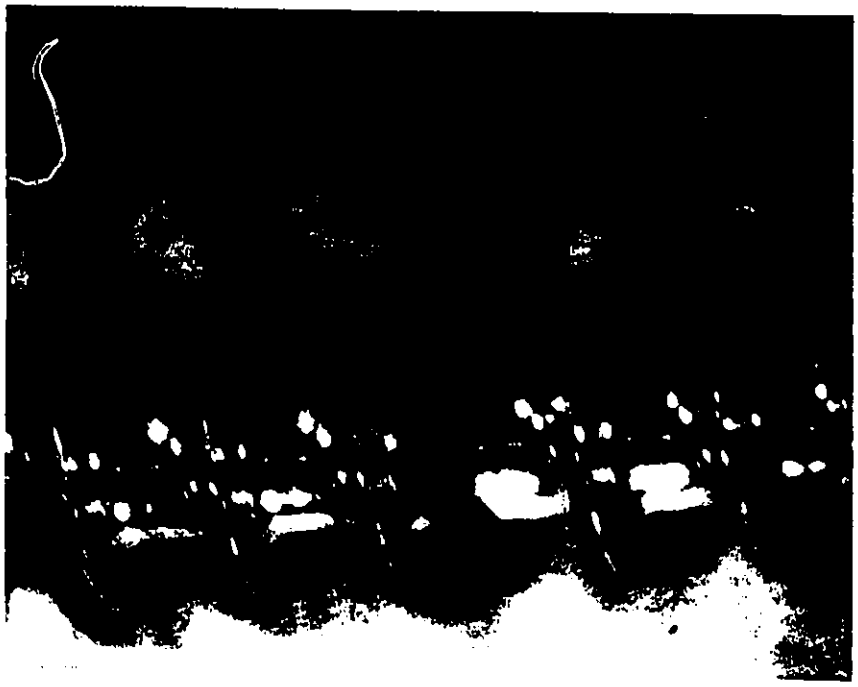

Test Coupon #7 4.0mm root diameter ; cycles to failure N=68,380

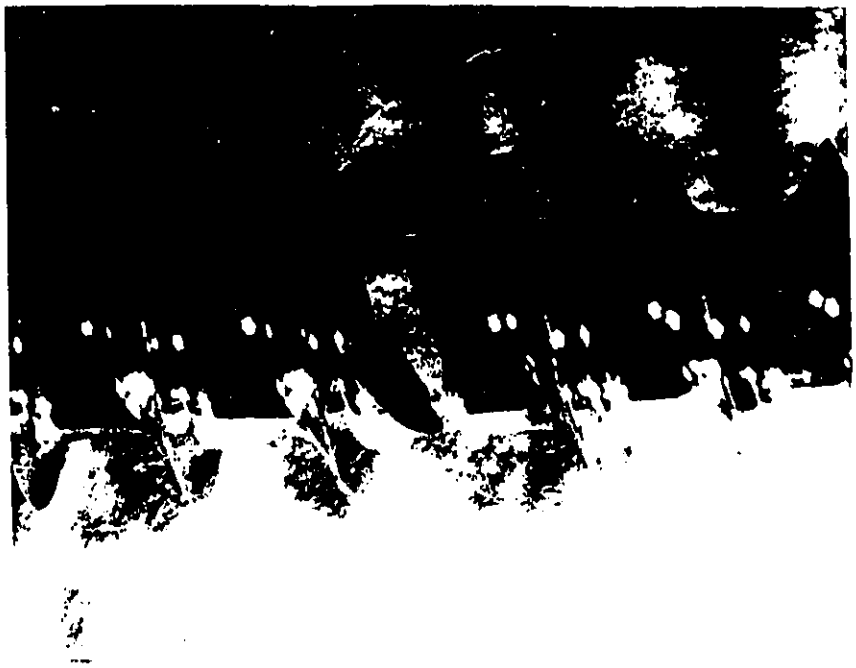

Test Coupon #9 4.0mm root diameter ; cycles to failure N=294,210

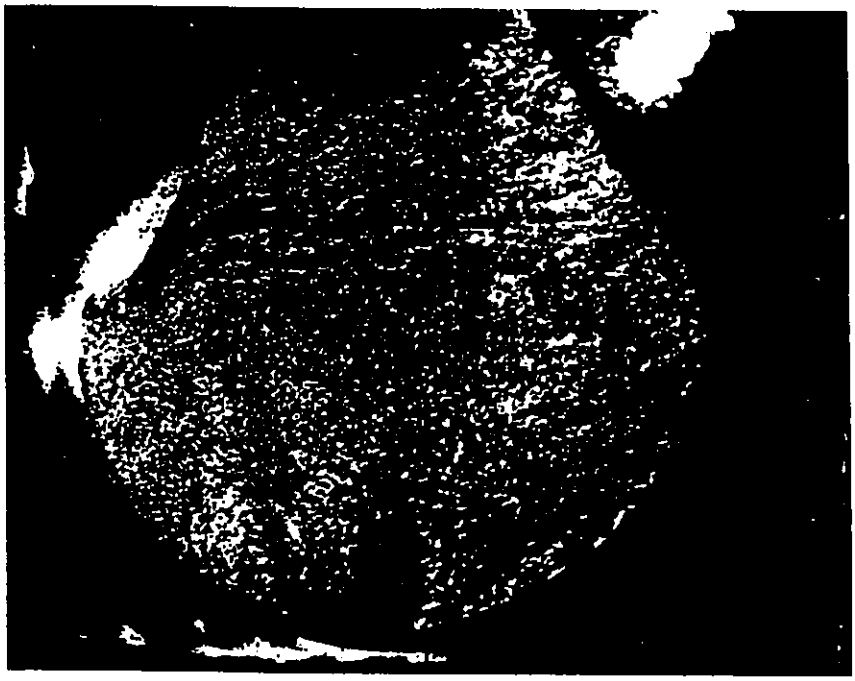

Test Coupon #9 4.0mm root diameter ; cycles to failure N=294,210

Test Coupon #10 4.0mm root diameter ; cycles to failure N=526,930

Test Coupon #10 4.0mm root diameter ; cycles to failure N=526,930

APPENDIX 9.0

EFFECT OF COLD WORK ON TENSILE PROPERTIES OF TYPES 316 AND 317

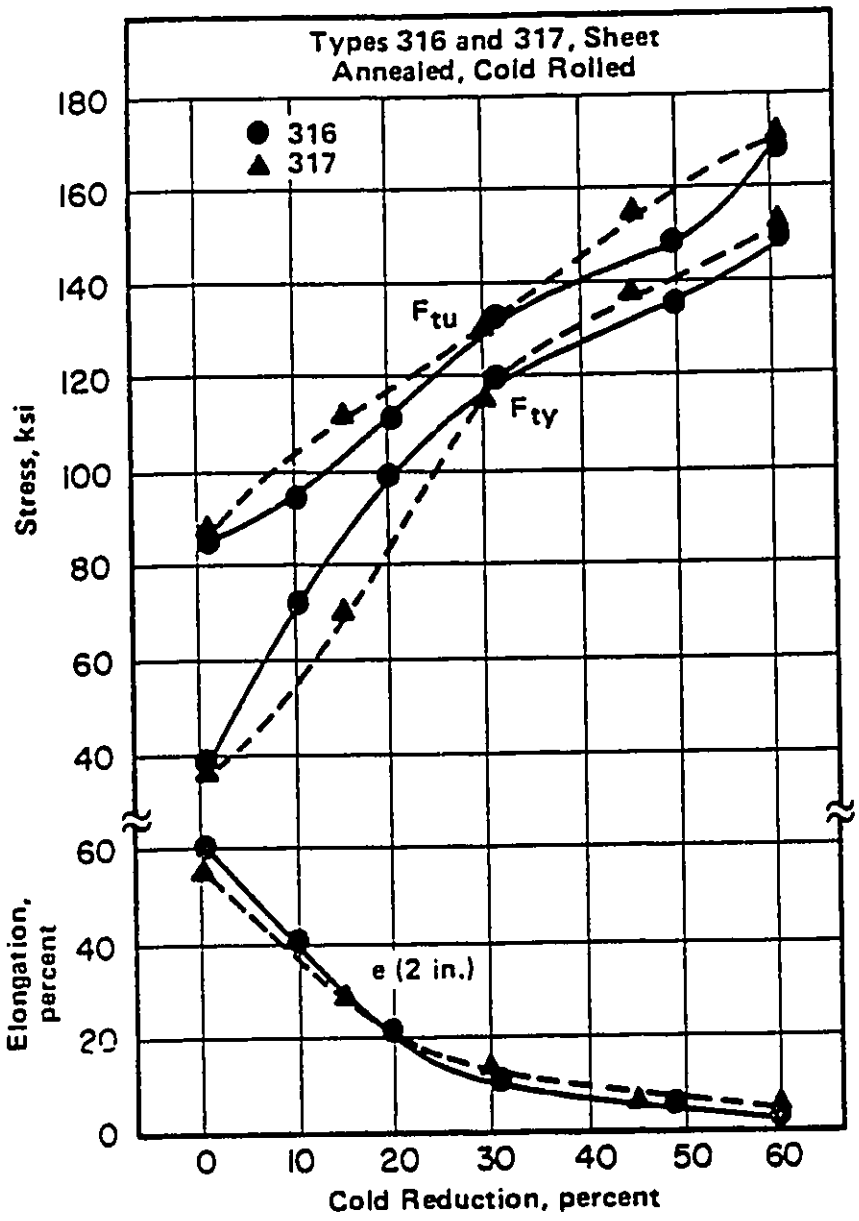
Types 316 and 317, Sheet
Annealed, Cold Rolled
316
317
F_{tu}
F_{ty}
e (2 in.)
Stress, ksi
Elongation, percent
Cold Reduction, percent
180
160
140
120
100
80
60
40
60
40
20
0
0
10
20
30
40
50
60